



Spatiotemporal Monitoring of Land Use-Land Cover and Its Relationship with Land Surface Temperature Changes Based on Remote Sensing, GIS, and Deep Learning

Razieh Karimian¹ · Kazem Rangzan¹ · Danya Karimi¹ · Golzar Einali²

Received: 2 February 2023 / Accepted: 23 July 2024
© Indian Society of Remote Sensing 2024

Abstract

Over the past century, rapid population growth and continuous exploitation of natural resources have caused numerous changes. A notable transformation involves the modification of land surface temperature (LST), which is impacted by changes in Land Use-Land Cover (LULC). The most important approach in discovering changes is to increase the accuracy of classification methods. Deep learning techniques have been successfully used, and this improved performance has been carried over to image classification. This study aims to monitor and mapping the spatial and temporal changes of LULC and LST in Izeh city using remote sensing, GIS, and deep learning. LULC and LST maps for the years 2001 and 2021 were created by processing thermal and multispectral bands. Two methods were used to generate the land use-land cover map: pixel-based (Max Likelihood (ML)) and object-based (Fully Convolutional Network (FCN)). During this period, the percentages of changes in water, urban, and wasteland classes increased, whereas those for grassland, forest, and wetland classes decreased. The average LST changes followed this order: wasteland > urban > grassland > forest > wetland > water. The normalized differential vegetation index (NDVI), normalized differential water index (NDWI), and normalized differential build-up index (NDBI) were utilized to analyze the relationship between LST and LULC. A linear, positive relationship between LST and NDBI was observed, indicating the direct effect of urban development on the increase in LST in the study area. The overall accuracy for LULC maps using the ML method was over 80.74% in 2001 and over 90.76% in 2021. With the FCN method, the accuracy was over 93% in 2001 and over 98% in 2021. Finally, evaluation the spatiotemporal environmental effects of unchecked human activity on LULC and its relationship with LST can be achieved using remote sensing, GIS, and deep learning approaches.

Keywords Deep learning (DL) · Fully convolutional network (FCN) · GIS · Land surface temperature (LST) · Land use-land cover (LULC) · Max likelihood (ML)

Introduction

Due to natural and human activities, the Earth's surface undergoes constant change (Grimm et al., 2008; John et al., 2020). Land surface changes generally fall into two categories: land use and land cover (Barnsley et al., 2001). According to Lambin and Ehrlich (1997), three main factors influence land use and land cover (LULC) change: institutional-political factors, biophysical factors, and technical and economic concerns. Nowadays, satellite images are commonly used to monitor spatial-temporal changes in LULC. Consequently, the causes and effects of changes related to human activity can be assessed (El-Zeiny & Effat, 2017). Remote sensing has numerous applications (Karimi et al., 2017a; b; Rangzan et al., 2022), including the discovery of

✉ Razieh Karimian
raziehkirimian1@gmail.com
Kazem Rangzan
kazemrangzan@scu.ac.ir
Danya Karimi
danya-karimi@stu.scu.ac.ir
Golzar Einali
golzar.einali@yahoo.com

¹ Department of Remote Sensing and Geographic Information System, Faculty of Earth Sciences, Shahid Chamran University of Ahvaz, Ahvaz, Iran

² Department of Remote Sensing and Geographic Information System, University of Tabriz, Tabriz, Iran

processes altered between different periods, which forms the core of change detection studies, and the detection of changes not discernible by ground observations (Lakra and Sharma, 2019; Imran et al., 2021). Remote sensing is particularly useful for monitoring and evaluating LULC changes, especially in areas significantly impacted by human activities. Satellite images with moderate spatial resolution, such as Landsat data (Williams et al., 2006), are commonly employed for observing and assessing LULC changes. Numerous studies, such as Lewinski (2006), Al Fugara et al. (2009), and Pal and Ziaul (2017), have investigated LULC changes using Landsat images.

The modification of Land Surface Temperature (LST) in an urban setting is one of the major effects of Land Use and Land Cover (LULC) change (Dhar et al., 2019; Gohain et al., 2021). Over the past decade, global environmental processes have been studied to understand climate change, utilizing LST as an excellent indicator to monitor the physical properties of surface processes and climate change. For this reason, LST is an important input for estimating the energy balance equation (Filgueiras et al., 2019). It has been concluded that the main sources of human heat emission in urban centers correspond to certain types of land use-land cover. Therefore, the ratio of different types of land use-land cover may significantly affect LST, especially the ratio of industrial and commercial areas. Thus, urban and industrial development emerges as one of the key contributors to the rise in temperatures. Consequently, the following discussion will focus on the research conducted on LST and land use change.

Yoo et al. (2019) utilized Convolutional Neural Network (CNN) and Random Forest (RF) methods with Landsat images to classify urban areas. Their study revealed that the CNN classifier achieved higher accuracy in class separation compared to RF (Yoo et al., 2019). In 2020, Soleimani et al. investigated the effects of land use changes on the temporal and spatial patterns of Land Surface Temperature (LST) and thermal islands in Saqqez city. In this research, they employed Landsat satellite images from 1989 to 2018. For classification, they utilized the maximum likelihood method, and subsequently, to extract temperature data, they applied the split window algorithm. Their results indicated an increase in thermal islands in the northeast of the city from 2008 to 2018. Moreover, the highest temperatures were observed in vegetation, residential, and wasteland areas. Overall, their findings demonstrated the direct effects of land use on temperature rise (Soleimani et al., 2018).

Das et al. (2021) investigated the effect of Land Use and Land Cover (LULC) on Land Surface Temperature (LST) in the Sansol region of India. In their study, they considered data from 1993 and 2018 to prepare the LULC and LST maps. The Kappa coefficient was employed to evaluate the accuracy of the LULC maps. The LST maps revealed an increase in temperature by 0.15 °C and 0.19 °C per year,

respectively, during summer and winter. The temperature rise was primarily attributed to urbanization, commercial activities, and coal mining regions. According to changes in the LULC pattern, urban areas expanded by 60%, while coal mining regions increased by 15%. The relationship between LST and various spatial indices such as the Normalized Difference Built-up Index (NDBI), Normalized Difference Vegetation Index (NDVI), and Normalized Difference Water Index (NDWI) was demonstrated through several correlations. Their findings indicated a negative association between LST and NDVI as well as LST and NDWI, whereas LST and NDBI showed a positive correlation. Finally, the simulation of temperature for the year 2041 suggested a potential rise of 0.21 °C per year in the forthcoming years (Das et al., 2021).

Although various classification algorithms have been applied in remote sensing studies, achieving high accuracy in detecting Land Use-Land Cover (LULC) changes remains a challenge. Previous studies have used various classification methods, such as Convolutional Neural Networks (CNNs) and Random Forest (RF), to improve the accuracy of LULC classification, revealing the superior performance of CNNs. The fully convolutional neural network approach and the Res-UNet model are used in our study to significantly improve the classification accuracy. This highlights the potential of deep learning to enhance change detection accuracy, addressing a critical research gap in the field. The purpose of this study is to evaluate and monitor Land Use and Land Cover (LULC) changes and their relation to Land Surface Temperature (LST) changes by integrating remote sensing, GIS, and deep learning techniques over the past 20 years (2001–2021) in Izeh city.

Study Area

Izeh city, covering an area of 4035 km², is situated in the northeastern part of Khuzestan province in southwestern Iran. The average annual rainfall is 670 mm, and the average daily temperature is 21 °C over a 20-year period (2001–2021). The study area extends spatially from 31° 26' 0" N to 32° 22' 0" N and 49° 32' 0" E to 50° 28' 0" E (Fig. 1). Over this twenty-year period, the highest recorded air temperature in July was 48 °C, while the lowest temperature in February reached 9 °C. The highest point in the region stands at 3589 m, and the lowest is 348 m above sea level. The climate of the Izeh plain is characterized as semi-humid and moderate. The plain is predominantly surrounded by limestone highlands (Asmari formation) and is geologically classified as an open karst plain, with two lakes named Miangan and Bandan (Moradi et al., 2020) present. The border of

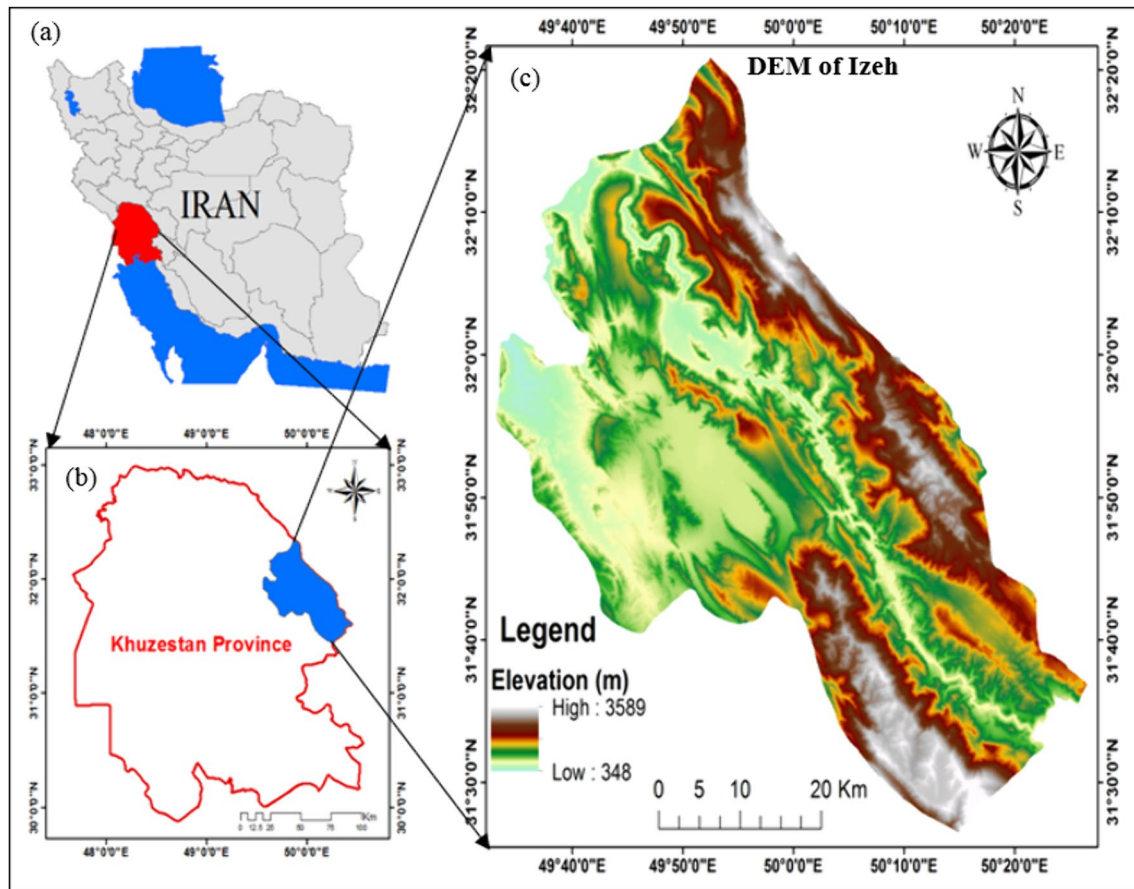


Fig. 1 Geographical location of the study area: Iran (a), Khuzestan (b), and the Digital Elevation Model (DEM) of Izeh (c)

the Izeh zone corresponds to the fronts of the Balaroud and Kazeroun mountains, situated across a distinct topographic gap in the southwest of the Zagros fault (Asadi Mehmandosti et al., 2013).

Materials and Methods

Materials/Datasets

Satellite Images

The present study utilized four Landsat images (path/row: 038/164 and 038/165) obtained for two distinct years from the Earth Explorer website of the USGS. Two images were selected from Landsat-7 ETM+ (for 2001) and two from Landsat-8 OLI/TIRS (for 2021), specifically for the months of August and September, considering minimal cloud cover (Amran et al., 2018). The details of the employed Landsat-8 images are provided in Table 1.

Table 1 Characteristics of the applied Landsat images

Satellite	Sensor	Row/Path	Year
Landsat 7	ETM+	164/038	2001
		165/038	
Landsat 8	OLI/TIRS	164/038	2021
		165/038	

Methodology

Image Pre-processing

Assuming that the spectral properties of non-changed areas remain stable, preprocessing is crucial in change detection studies. Inadequate preprocessing can lead to false change detection in the spectral space, increasing the risk of error (Wulder et al., 2006; Cooley et al., 2002). Prior to image processing, the preprocessing steps—radiometric control and image enhancement—were conducted (Aslami & Ghorbani, 2018).

An atmospheric correction tool called Fast Line-of-sight Atmospheric Analysis of Spectral Hypercube (FLAASH) is utilized to adjust remote sensor data in the 400 ± 3000 nm range (Jensen & Lulla, 1987). FLAASH employs MODTRAN simulations to generate spectral radiance data under different atmospheric, water vapor, and viewing conditions (solar angles) across various surface reflectances. These data are then utilized to create lookup tables for atmospheric parameters such as column water vapor, aerosol type, and visibility, which can be referenced for future analyses (Kruse, 2004; Adler-Golden et al., 2005; Pordel et al., 2019).

Land Use-Land Cover Map (LULC) Classification

In this study, two methods were employed for pixel-base classification: (a) The Maximum Likelihood Classifier (ML) and (b) the object-based Fully Convolutional Network (FCN), to classify the land use and land cover of the study area.

(a) Max Likelihood Classifier

Image classification categorizes pixels into different classes automatically (Lillesand et al., 2003). These classes can include urban, vegetation, water, and wasteland. Pixels are identified based on their spectral signatures, which reflect the relative reflectance of the area in various bands (Sabins, 1997). Among supervised classifiers, the Maximum Likelihood (ML) classifier is one of the most significant and accurate methods.

In this study, the LULC map was classified using the ML method in the ENVI software, which yielded the highest accuracy among the supervised classifiers (Lillesand et al., 2003). Training samples are required for each of these user-defined classes. The probability distribution of each class across the image is computed using the class means and covariances. Subsequently, each pixel is assigned to one of the classes based on its probability (Ayanlade & Howard, 2019).

According to the USGS definition, Land use-Land cover classes in the region include:

- **Water** streams, canals, lakes, reservoirs, bays, or oceans.
- **Wetland** mosaics of water, bare soil, and herbaceous or wooded vegetated cover.
- **Grassland** shrubs and perennial or annual natural and domesticated grasses (e.g., pasture), forbs, or other forms of herbaceous vegetation at least 10% of the area and tree cover is less than 10% of the area Pasture.
- **Forest** land spanning more than 0.5 hectares with trees higher than 5 m and a canopy cover of more than 10 percent.
- **Wasteland** natural occurrences of soils, sand, or rocks where less than 10% of the area is vegetated.

- **Urban** high-density residential, commercial, industrial, mining, or transportation.

We employed a random sampling method. The number of samples collected or selected for accuracy evaluation was calculated according to Professor Jensen's formula from the following Eq. (1):

$$N = \frac{Z^2 Pq}{E^2} = \frac{2^2(85)(15)}{5^2} = 204 \quad (1)$$

where $Z=2$, P is the required accuracy, $q=100-P$ and E is the acceptable error percentage. Therefore, the number of samples needed to determine the correct accuracy of the desired map was 204.

(b) Fully Convolutional Network (FCN) Structure

Numerous studies in machine learning, deep learning, and artificial intelligence have directed their attention toward diverse subjects, encompassing intelligent cities, weather forecasts, and change detection analysis (Elik and Gaziolu, 2020). Notably, Deep Learning has emerged as the predominant trend in image analysis, surpassing individual performance in challenging tasks (Torres et al., 2021).

CNN, a specific type of artificial neural network, is composed of convolutional layers, pooling layers, and fully connected layers (Yoo et al., 2019). The CNN approach has been widely successful in image classification. By incorporating fully connected layers, CNN can ascertain subsequent classification probability information. However, its application is limited to entire image classification, lacking pixel-level classification (Dai et al., 2016; Liu et al., 2020). Consequently, the Fully Convolutional Network (FCN) classification method was developed. This method transforms fully connected layers into convolutional layers, facilitating the creation of a classification network (Liu et al., 2020; Wu et al., 2021).

The FCN mainly consists of convolutional layers, an integration layer, and deconvolutional layers at its core. By semantically segmenting the data of the entire image, the FCN can classify pixels on a pixel-by-pixel level, significantly enhancing the algorithm's computing efficiency and accuracy (Wu et al., 2021). The FCN is utilized in the novel design of CNN models, which are configured as complete convolutional networks, optimizing the generation of proportionally sized outputs. This technique finds applications in tasks like edge detection (Xie and Tu, 2015; Ozturk et al., 2020; Wu et al., 2021), image classification (Yoo et al., 2019; Torres et al., 2021; Ghorbanzadeh et al., 2022), and more. An FCN can work with inputs of varying sizes, producing outputs with dimensions that match (potentially resampled) spatial dimensions. Furthermore, feedforward computation and backpropagation are considerably more effective when applied independently patch-by-patch across

the entire image, particularly when receptive fields significantly overlap (Ozturk et al., 2020).

In this study, the Keras open-source library was employed to implement the FCN. Various methods can be explored to construct the FCN architecture, necessitating the identification of an optimal model that suits the data's characteristics. To evaluate the image classes, an object-based image analysis (OBIA) approach was adopted, utilizing the probabilities derived from the ResU-Net model with a 50-backbone and Adam optimizer set at a learning rate of 0.001 (Ghorbanzadeh et al., 2022).

Utilizing open-source ALOS DEM data and Landsat 8 images from 2001 and 2021 for both training and testing the FCN model, we trained the FCN model using these images. The network architecture of the ResU-Net that we used consists of a total of 15 convolutional layers. We employed the binary cross entropy loss function to determine the difference between each of the highest probability 1. The applied patch size is 64*64 and the bath size is 128. For data augmentation of the training sample patches, we utilized horizontal and vertical data flips. The number of image patches became 6000, of which 4000 were selected as training data and 2000 as test data. Additionally, a rule-based OBIA approach was devised during the object-based classification stage, incorporating land use-land cover classes.

Evaluation Method of LULC

(a) Assessing the Accuracy of the ML Method.

In this study, accuracy is evaluated using the error matrix which contains information about actual and anticipated pixel identifications (Jupp, 1989; Pal & Ziaul, 2017). Equation 2 is used to calculate the overall accuracy.

$$T = \frac{\sum D_{ii}}{N} \quad (2)$$

In this formula, T represents the overall accuracy, $\sum D_{ii}$ signifies the number of pixels that are correctly classified, and N is the total number of pixels in the error matrix. Equation 3 is used to calculate the producer's accuracy, and the user's accuracy is calculated using Eq. 4.

$$PA = \frac{\sum D_{ij}}{R_i} \quad (3)$$

where $\sum D_{ij}$ represents the number of pixels in a row I that are correctly classified, R_i stands for the total number of pixels in a row i , and PA represents the producer's accuracy.

$$UA = \frac{\sum D_{ij}}{C_j} \quad (4)$$

where $\sum D_{ij}$ signifies the number of pixels in column j that are correctly classified, C_j represents the total number of pixels in column j , and UA represents the user's accuracy.

Another accuracy coefficient, known as the kappa coefficient (Foody, 1992), was used in this research. The Kappa coefficient's value ranges between 0 and 1, where 0 indicates weak agreement, and 1 indicates almost complete agreement (Landis & Koch, 1977) (Fig. 2).

(b) Assessing the Accuracy of the FCN Method

Common metrics for image classification tasks include accuracy, precision, recall, F1 score, confusion matrix, and area under the receiver operating characteristic curve (AUC-ROC). In this study accuracy, precision, and F1 score criteria were used to evaluate the accuracy of the FCN method and the theRes-UNet model.

Accuracy measures the proportion of correctly classified instances compared to the total instances. It's computed by dividing the number of correct predictions by the total number of predictions. While accuracy offers a comprehensive performance assessment, it may not suffice for datasets with imbalanced classes (Useya & Chen, 2018). Precision evaluates the ratio of true positive predictions among all positive predictions, calculated by dividing true positives by the sum of true positives and false positives. Precision is valuable when false positives are costly (Theres & Selvakumar, 2022). The F1 Score, a harmonic mean of precision and recall, balances both metrics and proves beneficial when considering false positives and false negatives. It's calculated as $2 * ((\text{precision} * \text{recall}) / (\text{precision} + \text{recall}))$ (Chakhar et al., 2020).

Change Detection Method

The LULC classification for 2001 and 2021 was compared utilizing the change matrix, following the methodology proposed by Weng et al. (2004), within the ArcGIS 10.7 software. To detect changes, a combination of qualitative and quantitative techniques was employed. After identifying the change matrix, a map of changes was generated in the ArcGIS environment using spatial analysis tools.

LST Estimation Methods from the Thermal Band

Temperature data is collected by Landsat sensors (ETM+ and OLI) and stored as digital numbers (DN) within a range of 0–255. For meaningful comparisons, all included images were captured during the same season and nearly simultaneously (Coll et al., 2010). Land Surface Temperature (LST) is derived using the thermal bands of Landsat 7 ETM+ (band 6) and Landsat 8 OLI (band 10). However, the LST extraction process from Landsat ETM+ and Landsat OLI calculates spectral radiance ($L\lambda$) in distinct ways (Asgarian et al., 2014; Nguemhe Fils

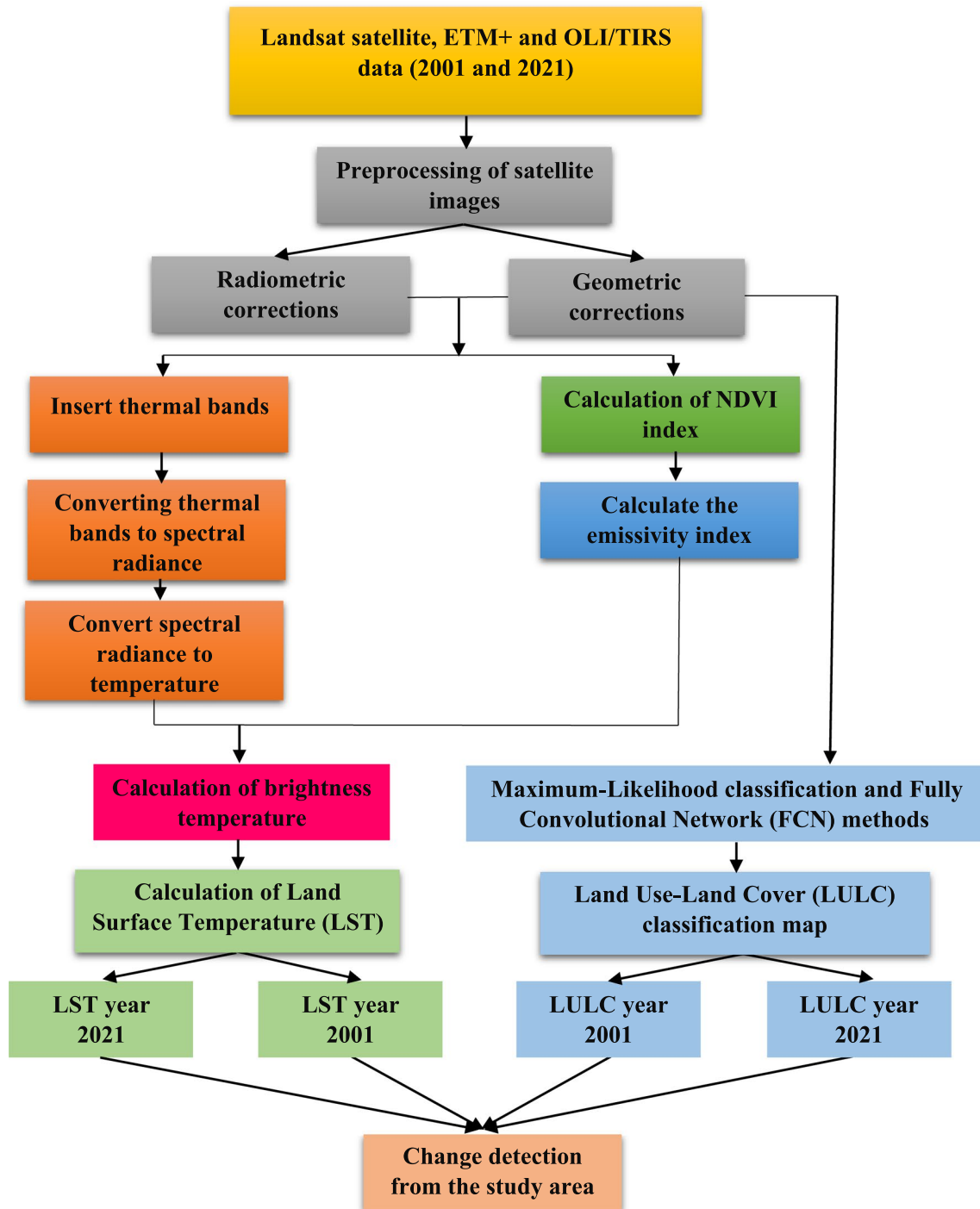


Fig. 2 Flowchart of the current study

et al., 2017). The steps for extracting LST from Landsat images are outlined below (Govind & Ramesh, 2019).

Step 1: Convert DN to Spectral Radiance ($L\lambda$).

The spectral radiance of the upper atmosphere ($L\lambda$) is calculated using Eq. 5, which involves ETM + band six for Landsat 7.

$$L\lambda = LMIN\lambda + \left[\frac{LMAX\lambda - LMIN\lambda}{QCALMAX\lambda - QCALMIN\lambda} \times QCAL \right] \quad (5)$$

For each pixel, QCALMIN is set to 1, while QCALMAX is set to 255. The spectral radiance for band six is denoted

by $L_{MAX\lambda}$, with a value of 15.303, and $L_{MIN\lambda}$, with a value of 1.238. QCAL represents the numerical value of each pixel.

On Landsat 8, the thermal band is designated as OLI band 10, and the extraction of spectral radiance ($L\lambda$) is accomplished using Eq. (6).

$$L\lambda = ML \times QCAL + AL \tag{6}$$

Here, $L\lambda$ represents the upper spectral radiance of the atmosphere, ML stands for the band-specific multiplicative scaling factor (0.0003342), AL is the band-specific incremental scaling factor (0.1), and QCAL signifies the pixel value of the standard quantized and calibrated product (Das et al., 2021).

Step 2: Converting Spectral Radiance to Brightness Temperature (BT)

Brightness temperature, also known as apparent temperature, corresponds to the temperature of the blackbody that produces the radiation captured by the sensor. It is also the temperature received by satellites. It's important to note that brightness temperature doesn't directly represent the actual temperature of the Earth; instead, it reflects the temperature of the satellite itself. Consequently, the data from Landsat's thermal bands can be transformed from spectral radiance to brightness temperature (Eq. 7). This conversion is achieved using the thermal constants provided within the metadata file (Sherafati et al., 2018; Ibrahim and Mallouh, 2018).

$$BT = \frac{K_2}{\ln\left[\left(\frac{K_1}{L_\lambda} + 1\right)\right]} \tag{7}$$

In this context, BT denotes the brightness temperature of the satellite in Kelvin, while $L\lambda$ represents the spectral radiance recorded by the sensor ($W/m^2 \cdot sr \cdot \mu m$). K_1 stands for the constant coefficient of the first calibration ($W/m^2 \cdot sr \cdot \mu m$), and K_2 represents the constant coefficient of the second calibration ($W/m^2 \cdot sr \cdot \mu m$).

Step 3: Emissivity Index (ϵ)

The method proposed by James and Sobrino was employed to calculate emissivity. Emissivity is derived through thresholding the NDVI index (Eq. 8).

$$PV = \left[\frac{NDVI - NDVI_{min}}{NDVI_{max} - NDVI_{min}} \right]^2 \tag{8}$$

The emissivity index (ϵ) is obtained using the following Eq. (9) (Das et al., 2021).

$$\text{Land Surface Emissivity } (\epsilon) = 0.004 \times PV + 0.986 \tag{9}$$

Step 4: Calculate the Land Surface Temperature

In this step, we determine the Atmospheric Water Vapor Index (AWVI) and the temperature of the Earth's surface using the single-channel algorithm.

For estimating the Land Surface Temperature (LST) using the single-channel method, it's crucial to ascertain the atmospheric water vapor content during the satellite's passage. The atmospheric water vapor was determined using the following Eq. (10), which incorporates meteorological information to derive the relative humidity (Nasseri, 2019).

$$\begin{aligned} \omega_i &= 0.0981 \\ &\times \left\{ 10 \times 0.6801 \times \exp \left[\frac{17.27 \times (T_0 - 273.15)}{273.15 + (T_0 - 273.15)} \right] \times RH \right\} \\ &+ 0.167 \end{aligned} \tag{10}$$

In this context, T_0 represents the temperature of the air near the Earth's surface, RH stands for the relative humidity of the air, and ω_i signifies the atmospheric water vapor content.

The single-channel algorithm employs thermal infrared bands to extract the Land Surface Temperature (LST). This approach is applicable to sensors equipped with a thermal band (bands 10 and 11) (Chatterjee et al., 2017).

$$T_s = \gamma \left[\epsilon^{-1} (\varphi_1 L_{sensor} + \varphi_2) + \varphi_3 \right] + \delta \tag{11}$$

$$\gamma = \left\{ \frac{C_2 L_{sensor}}{T_{sensor}^2} \left[\frac{\lambda^4}{C_1} L_{sensor} + \lambda^{-1} \right] \right\}^{-1} \tag{12}$$

Here, T_s signifies the Land Surface Temperature (LST), T_{sensor} stands for the sensor's brightness temperature in Kelvin, ϵ represents surface emissivity, γ denotes the effective wavelength of a thermal infrared band, while γ and δ are parameters tied to the Planck function. Additionally, φ_1 , φ_2 , and φ_3 are atmospheric correction parameters (Eqs. 11 and 12). By applying these parameters, the atmospheric influence is significantly mitigated or adjusted, a calculation achieved through the utilization of the following Eqs. (13, 14, 15, 16, and 17). It's important to note that all parameters are wavelength-dependent (Munoz et al., 2009). The value of C_1 is $1.19104 \times 10^8 W \cdot m^{-2} \cdot sr^{-1} \cdot \mu m^4$, and the value of C_2 is $14,387.7 \mu m \cdot K$.

$$\begin{bmatrix} \varphi_1 \\ \varphi_2 \\ \varphi_3 \end{bmatrix} = \begin{bmatrix} C11 & C12 & C13 \\ C21 & C22 & C23 \\ C31 & C32 & C33 \end{bmatrix} \begin{bmatrix} \omega^2 \\ \omega \\ 1 \end{bmatrix} \tag{13}$$

In the equation mentioned above, the C coefficients are acquired through simulation.

$$\varphi = -\gamma L_{sensor} + T_{sensor} \tag{14}$$

Table 2 The area of each LULC (Km²)

Land Use-Land Cover class	Area of 2001 (Km ²)	Area of 2021 (Km ²)
Water	33,201.64	35,851.13
Urban	5374. 81	5604.851
Wasteland	219,369.05	238,147.04
Grassland	60,833.90	57,424.16
Wetland	2499.78	2377.04
Forest	69,302.65	67,175.09
Total (Km ²)	385,207.02	406,579.311

$$\varphi_1 = 0.14714\omega^2 - 0.15583\omega + 1.1234 \tag{15}$$

$$\varphi_2 = -1.1836\omega^2 - 0.3760\omega - 0.52894 \tag{16}$$

$$\varphi_3 = -0.04554\omega^2 + 1.8719\omega - 0.39071 \tag{17}$$

Calculating Spatial Indices

(a) Normalized Differential Vegetation Index (NDVI)

The Normalized Difference Vegetation Index (NDVI) is a numerical indicator that utilizes the visible and near-infrared

bands of the electromagnetic spectrum. It evaluates whether an observed target contains living vegetation. NDVI values range from - 1 to + 1. As values approach + 1, they indicate a higher presence of vegetation, while values associated with water and clouds are generally below zero. This is calculated using the following Eqs. (18) (Kayet et al., 2016).

$$NDVI = \frac{NIR - Red}{NIR + Red} \tag{18}$$

NIR indicates the extent of reflection in the infrared band, while *Red* indicates the degree of reflection in the red band.

(b) Normalized Differential Water Index (NDWI)

NDWI is an additional index utilized to demarcate open water boundaries and identify them using remote sensing data based on near-infrared and visible radiation. The following Eq. (19) can be employed to calculate NDWI (McFeeters, 1996):

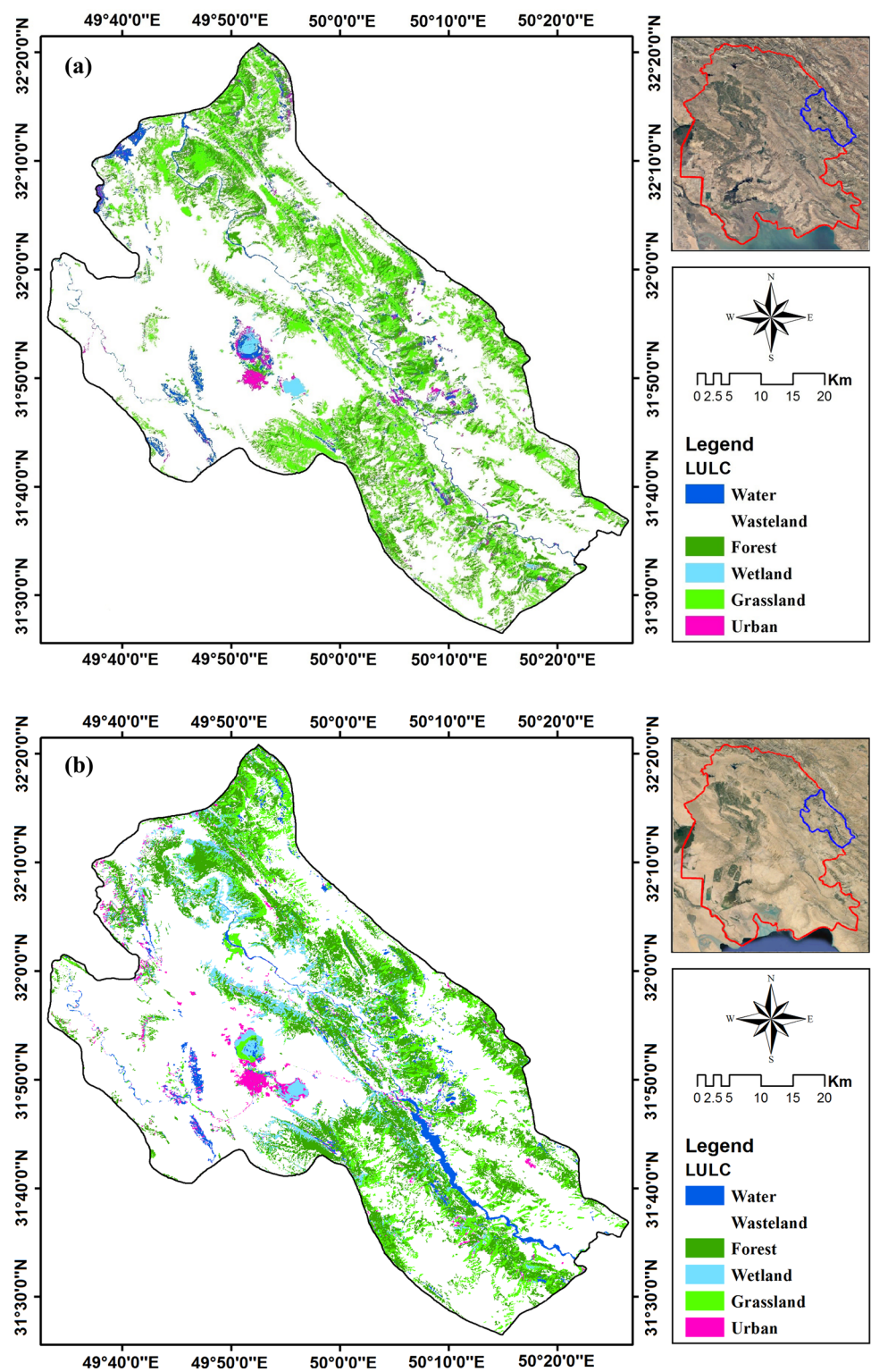
$$NDWI = \frac{Green - NIR}{Green + NIR} \tag{19}$$

Green refers to band 2 for Landsat 7 (ETM+) images and band 3 for Landsat 8 (OLI) images. Near-infrared (NIR) corresponds to band 4 for Landsat ETM+ and band 5 for Landsat OLI images. Smaller values, including negative values, indicate the presence of vegetation, whereas NDWI values

Table 3 Assessment of the accuracy of LULC in 2001 and 2021

Year	Class type classified by Landsat images of Izeh city							Total	User's accuracy	Kappa coefficient	
	LULC	Water	Wasteland	Forest	Wetland	Grassland	Urban				
2001	Water	186	2	0	11	4	1	204	98.4	0.77	
	Wasteland	2	189	0	0	11	2	204	82.17		
	Forest	1	3	161	2	36	1	204	81.63		
	Wetland	0	6	0	187	6	11	204	77.39		
	Grassland	0	9	36	2	134	23	204	67.68		
2001	Urban	0	21	0	42	28	93	204	75.82		
	Total	189	230	197	244	219	131	950			
	Producer' accuracy	91.09	92.65	78.82	88.56	56.37	58.97				
	Overall accuracy	80.74%									
2021	Water	200	2	0	1	0	1	204	99.24	0.88	
	Wasteland	1	199	1	0	0	3	204	97.59		
	Forest	0	1	201	0	2	0	204	98.62		
	Wetland	0	0	0	204	0	0	204	97.07		
2021	Grassland	0	0	2	0	185	0	204	98.83	0.99	
	Urban	0	16	0	0	0	188	204	93.62		
	Total	201	218	204	205	187	202	1177			
	Producer' accuracy	99.37	98.14	99.42	100	98.83	92.07				
	Overall accuracy	90.76%									

Fig. 3 LULC map of 2001 (a) and 2021 (b) of Izeh city



exceeding 0.5 signify water bodies. Thus, water bodies can be readily distinguished from vegetation. Values ranging from 0 to 0.2 are typically associated with human-made areas (Das et al., 2021).

(c) Normalized Differential Build-up Index (NDBI)

By utilizing the mid-infrared (MIR) and near-infrared (NIR) bands, we can calculate this index using remote sensing data. The equation provided below (20) was employed to compute the Normalized Difference Built-Up Index (NDBI) (Zha et al., 2003).

Table 4 Accuracy assessment of ResU-Net method for classification Images of the study area

	Class	Precision	Reclass	F1-score	Accuracy
2001	Class1	1.00	0.92	0.96	0.93
	Class2	0.99	0.84	0.91	
	Class3	0.97	0.99	0.98	
	Class4	0.84	0.92	0.88	
	Class5	0.97	1.00	0.99	
	Class6	0.61	0.40	0.49	
2021	Class1	0.98	0.98	0.98	0.98
	Class2	1.00	0.98	0.99	
	Class3	0.95	0.95	0.95	
	Class4	0.92	0.87	0.89	
	Class5	1.00	1.00	1.00	
	Class6	0.85	0.91	0.88	

$$NDBI = \frac{MIR - NIR}{MIR + NIR} \quad (20)$$

Here, *MIR* refers to the mid-infrared band (band 5 for Landsat ETM+ and band 6 for Landsat OLI), while *NIR* corresponds to the near-infrared band (band 4 for Landsat ETM+ and band 5 for Landsat OLI). NDBI values span from -1 to +1, where the range of 0 to 1 is associated with urban

areas. A value around 1 indicates a dense concentration of built-up regions (Choudhury et al., 2019).

Evaluation of the Relationship Between the LST and Spatial Indicators

To understand the influence of different spatial characteristics on Land Surface Temperature (LST), Pearson's correlation function within the SPSS statistical package was employed. In this study, raster correlations, such as those between LST and NDVI, LST and NDWI, etc., were visualized using Saga software (as detailed in the results and discussion section).

Results and Discussion

Land Use-Land Cover Results

Results of the ML Classifier

The LULC maps of the study area were classified into six classes: water, urban, wasteland, grassland, wetland, and forest. Table 2 presents the area of each LULC class for both 2001 and 2021. To assess the accuracy of the LULC maps, ground observation points were collected with the assistance

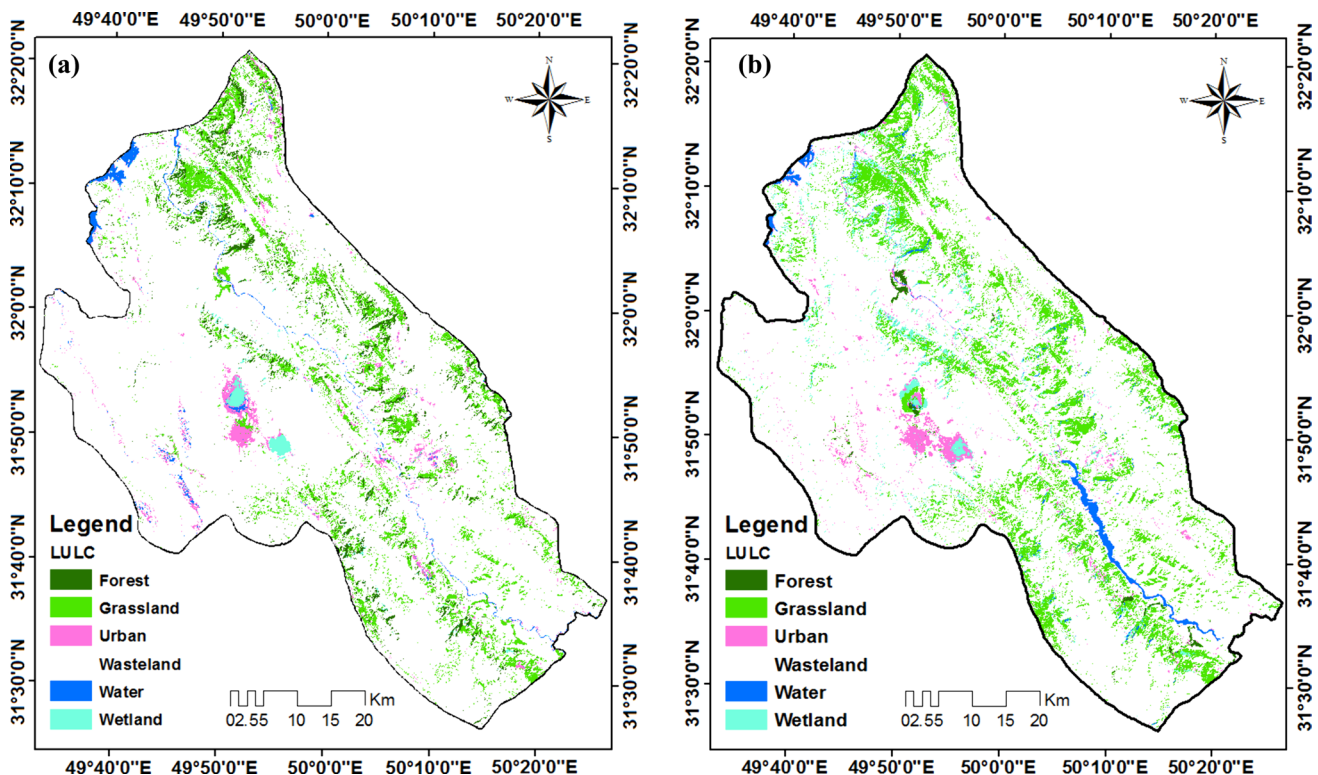


Fig. 4 The LULC map of 2001 (a) and 2021 (b) of Izeh city using the FCN approach

Table 5 Percentage changes of LULC from 2001 to 2021

LULC class	Changes percentage (%)
Water	7.98
Wasteland	8.56
Forest	- 3.07
Wetland	- 4.91
Grassland	- 5.605
Urban	4.28

of Google Earth. The accuracy of the LULC maps was also analyzed using the Kappa coefficient. The Kappa coefficient values were 0.77 for 2001 and 0.88 for 2021 (Table 3), indicating both LULC classifications were achieved with acceptable accuracy.

In 2001, the area of the water class was 33,201.64 km² (Fig. 3a and b). However, by 2021, it had expanded to 35,851.13 km² due to the construction of the Karun 3 dam and the formation of its associated lake. Observing the distribution of settlements, it's evident that in 2001, they were primarily concentrated in the central core of Izeh city. However, by 2021, settlements had expanded, leading to urban and rural area development (Fig. 5).

The area of wastelands in 2001 measured 219,369.05 km², which slightly decreased to 238,147.04 km² by 2021. Wetlands in the region also exhibited a decreasing trend, declining from 2499.78 km² in 2001 to 2377.04 km² in 2021. Over the past two decades, areas covered by dense vegetation, such as forests, have decreased from 69,302.65 to 67,175.09 km² within the study area (Table 2, Figs. 5 and 6).

Results of the FCN Model

Subsequently, the land use detection maps generated through the integrated approach and the FCN model were validated using precision, recall, and standard score performance measures.

Table 4 shows the evaluation of the FCN method for the classification of regional images. As can be seen in Table, the highest resulting accuracy scores for the LULC map of 2001 and 2021 were 93% and 98%, respectively. These values were obtained using a window size of 128 × 128 for generating sample patches.

F1-score was used to evaluate the classification accuracy of the FCN method. This criterion is calculated based on the precision and recall of the classifier, where precision is the ratio of the number of true positive samples to the total number of samples predicted positive, and recall is the ratio of the number of true positive samples to the total number of positive samples. The highest possible value for F1-score is 1 and the lowest possible value for

this criterion is 0. F1-score was calculated for each class showing that the number of positive samples correctly recovered is close to 1.

As a result, utilizing the FCN method and the theRes-UNet model yields higher accuracy compared to pixel-based methods such as Max-Likelihood. This supervised learning model can effectively differentiate between the characteristics of the six classes of the region and accurately separate (Fig. 4).

Change Detection of LULC

Table 5 illustrates the positive and negative changes within the six classes of the study area's LULC. Water bodies, urban areas, and wastelands have experienced positive changes, while forests, wetlands, and grasslands have undergone negative changes (Table 5). A positive change signifies an increase in the area of LULC, whereas a negative change denotes a decrease.

Residential areas have experienced a 4.28% increase due to urban expansion, resulting in a reduction in agricultural and wasteland areas (Fig. 6). Notably, the wetlands area, including Miangaran and Bandan wetlands, has decreased by 4.91% (Figs. 5, 6; Table 5). A graphical representation of the changes in each LULC class is provided in Fig. 6.

Land Surface Temperature Changes

Land Surface Temperature (LST) maps were extracted for 2001 and 2021 (Fig. 7a and b). In 2001, the recorded LST ranged from a high of 58 °C to a low of 18 °C. In contrast, for 2021, there was a decrease in the maximum temperature and an increase in the minimum temperature. Specifically, the maximum temperature reached 55 °C, while the minimum temperature rose to 20 °C. Consequently, it was observed that the maximum temperature decreased by 3 °C, while the minimum temperature increased by 2 °C (Table 6).

Distinct patterns of Land Surface Temperature (LST) are closely linked to the thermal characteristics of different Land Use and Land Cover (LULC) classes (Weng Q., 2004). To comprehend how LULC influences LST, thermal values were obtained for each land use category. Figure 8 displays the temporal and spatial variations of LST for Izeh city.

The minimum average LST levels were observed for water bodies, wetlands, forests and grasslands (in 2001: 32.02 °C for water bodies, 33.01 °C for wetlands, 33.85 °C for forests and 34.92 for grasslands, and in 2021: 30.11 °C for water bodies, 31.49 °C for wetlands, 33.06 °C for forests and 34.6 for grasslands).

Conversely, the maximum average LST levels were recorded for wastelands and urban areas (in 2001 37.54 °C

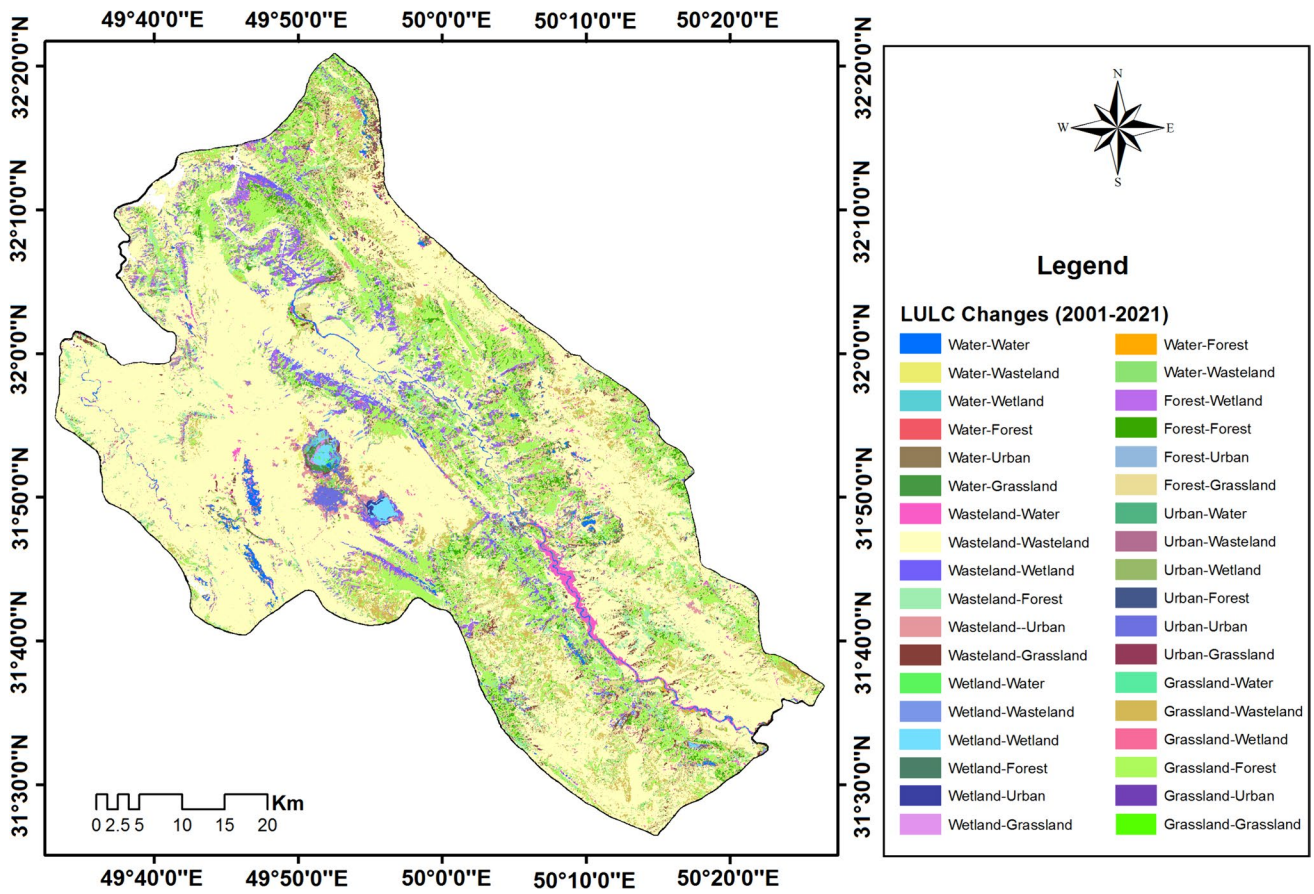


Fig. 5 Map of LULC changes in Izeh city from 2001 to 2021

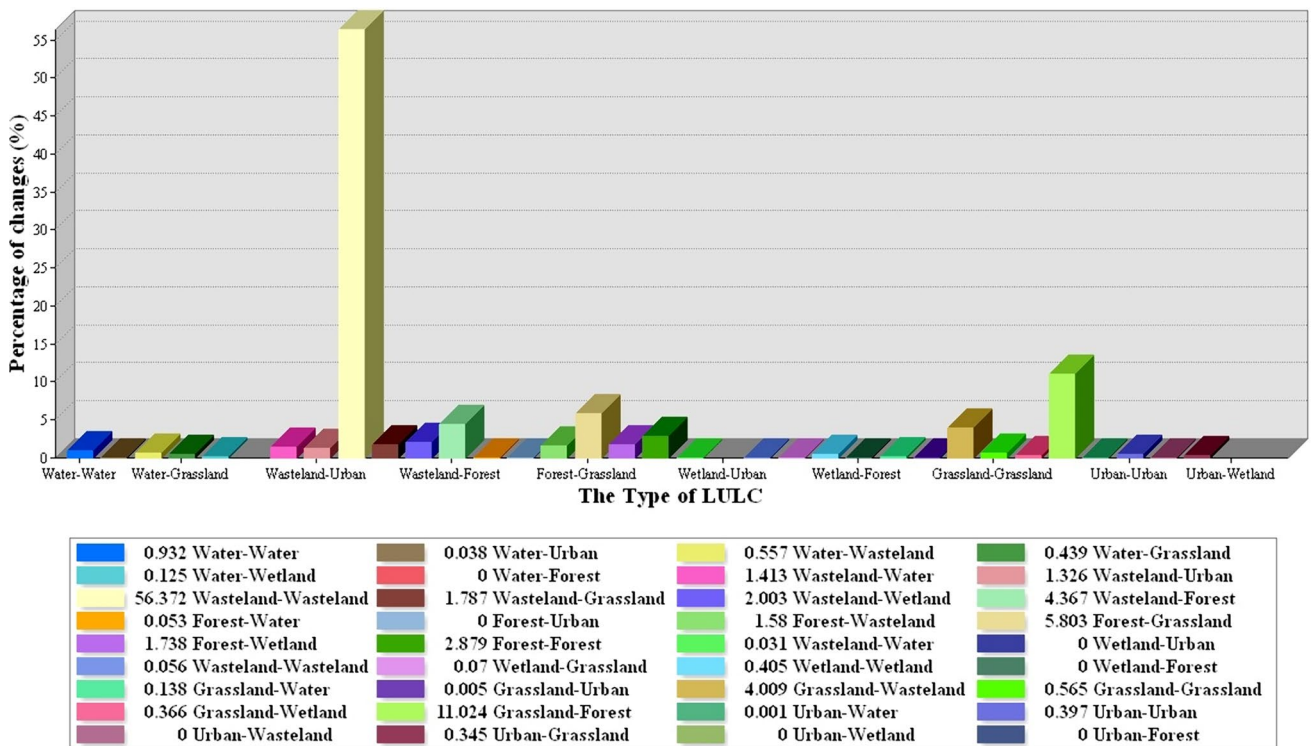


Fig. 6 The graph of changes in each LULC class from 2001 to 2021 in the study area

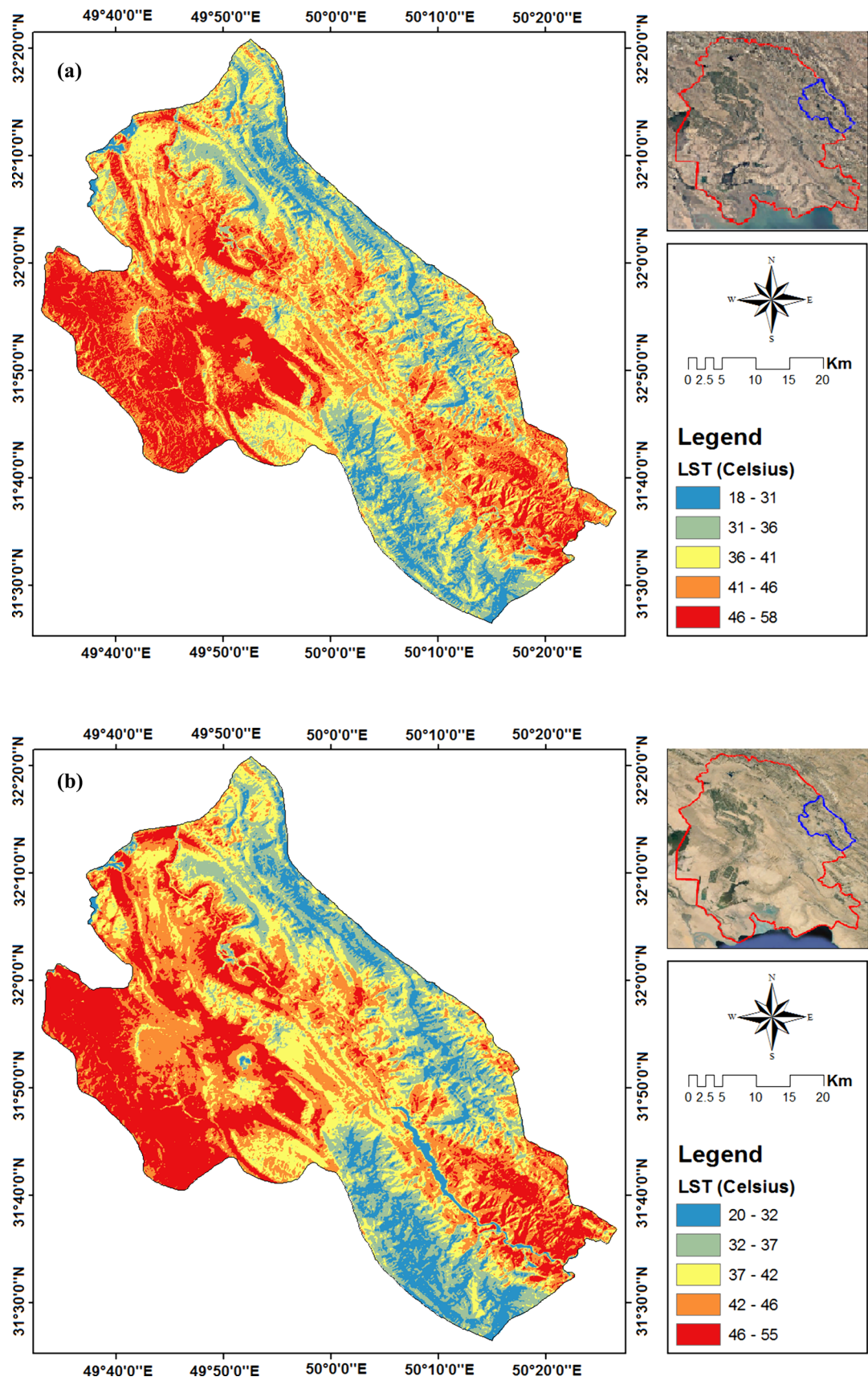


Fig. 7 LST map of the years 2001 (a) and 2021 (b) of Izeh city

Table 6 Statistics of changes in the LST from 2001 to 2021

Year	Maximum temperature (°C)	Minimum temperature (°C)	Average temperature (°C)
2001	58	18	38
2021	55	20	37.5

for wastelands, and 36.53 °C for urban areas, and in 2021, 44.37 °C for wastelands, and 40.11 °C urban areas (Figs. 8, 9 and Table 7).

Figure 9 illustrates the average LST changes for each land use class over the twenty-year period, following this order: wasteland > urban > grassland > forest > wetland > water (as presented in Table 7, Figs. 8, and 9). The increase in LST between 2001 and 2021 can be attributed to urban development and wasteland expansion in Izeh city. Additionally, the analyses indicate that water bodies exhibit lower LST levels.

Interestingly, despite the high recorded LST being associated with forests, the digital elevation model (DEM) of

the study area reveals that the forested regions are situated at higher altitudes. Moreover, observations suggest that the influence of altitude on LST outweighs that of vegetation (Aguilar-Lome, 2019). Consequently, the high LST observed in forested areas can be attributed to their elevated altitude within the study area.

The Influence of Water Bodies, Vegetation, and Urban Areas on LST

An analysis of correlations between Land Surface Temperature (LST) and factors such as vegetation, water bodies, and urban areas was conducted. The correlation between these factors and indices such as NDVI, NDWI, and NDBI was explored. Spatial distributions of NDVI in the study area are shown in Fig. 10a and b. Darker green regions indicate dense vegetation, while the purple color represents water bodies. In 2001, the northwestern and southwestern parts of Izeh city exhibited dense vegetation, while the western part displayed minimal vegetation due to urban and desert expansion. This relationship between NDVI and NDBI becomes evident.

Fig. 8 Map of LST changes in the study area from 2001 to 2021 using Landsat8 images

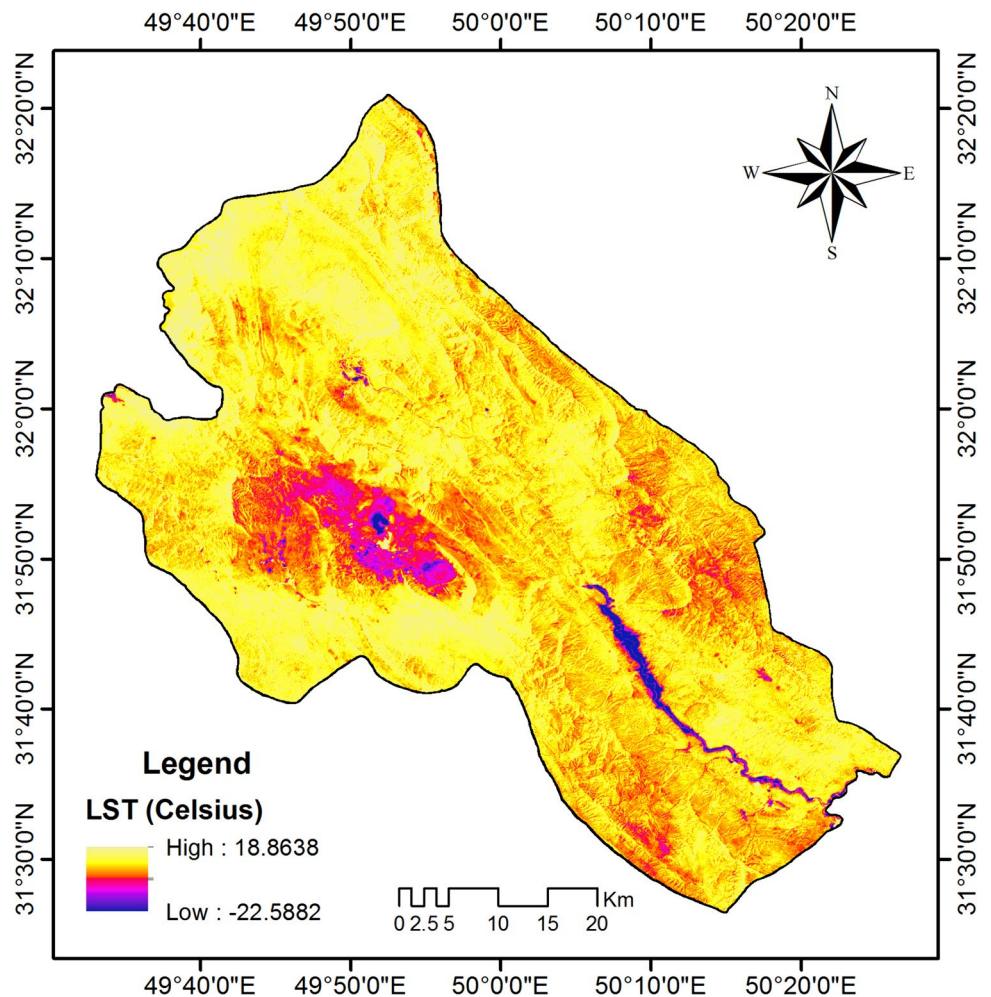


Fig. 9 The graph of the average temperature changes of the land surface for the LULC classes

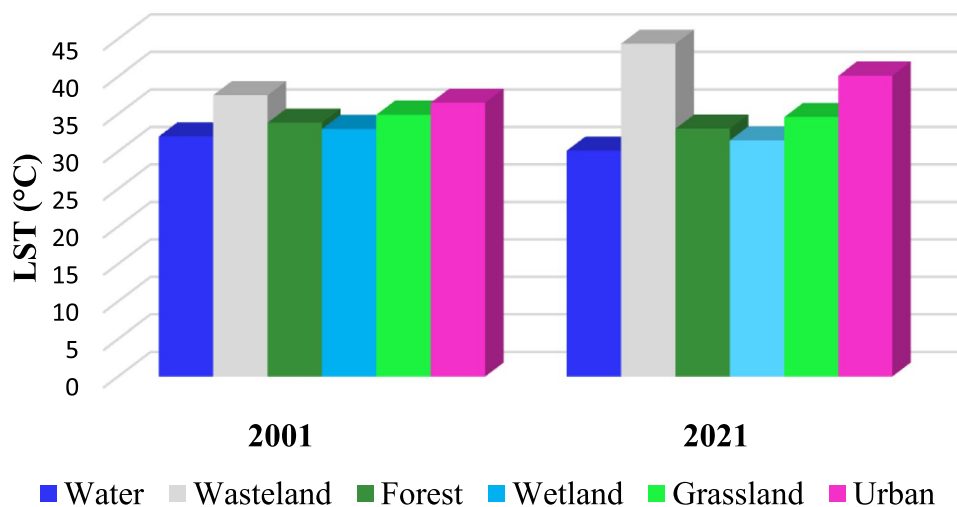


Table 7 Average LST changes (°C) for each LULC class

Land use-land cover class	2001	2021	Temperature difference
Water	32.02	30.11	-1.9
Wasteland	37.54	44.37	+6.83
Forest	33.85	33.06	-0.79
Wetland	33.01	31.49	-1.52
Grassland	34.92	34.6	-0.32
Urban	36.53	40.11	+3.85

Figure 11 depicts a weak negative association between NDBI and NDVI (correlation coefficient of -0.47), indicating that urban expansion leads to reduced vegetation cover. Both NDVI and LST show a negative correlation for 2001 and 2021, as displayed in Fig. 12a and b. This correlation is due to abundant vegetation preventing higher surface temperatures.

NDWI is another significant index negatively correlated with LST (correlation coefficient of -0.037, Table 8), primarily because water possesses a relatively high specific heat capacity (Moldoveanu & Minea, 2019) (Fig. 13).

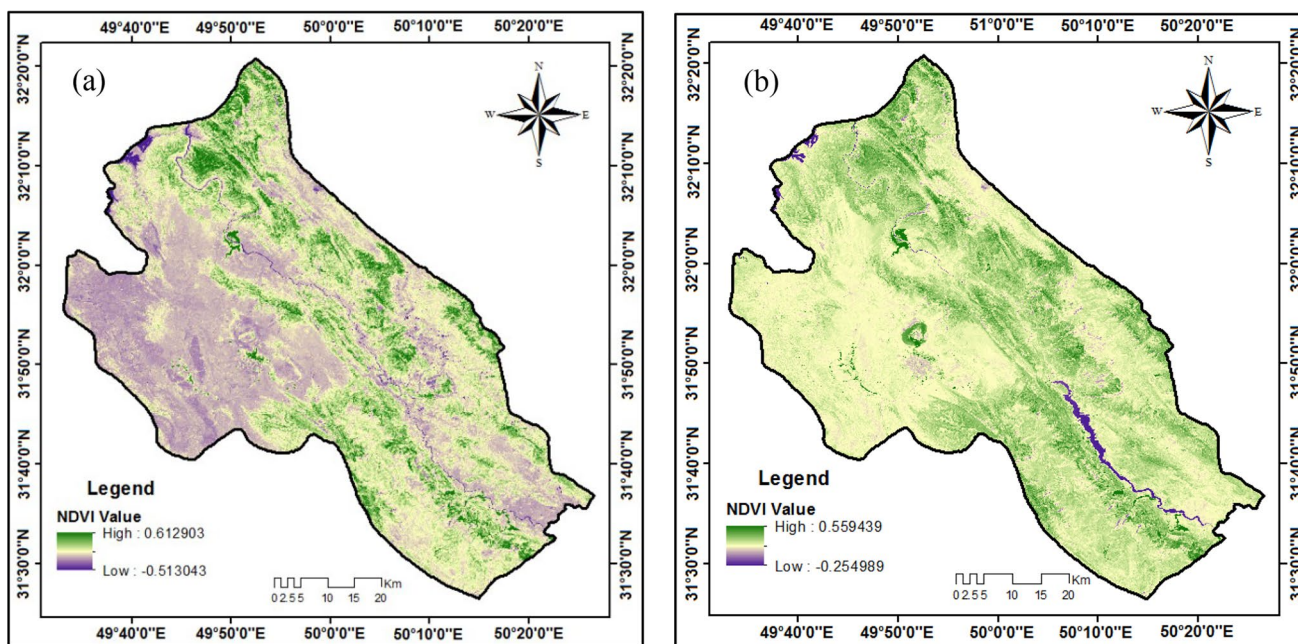


Fig. 10 Vegetation index map of the study area in 2001 (a) and 2021 (b)

Fig. 11 Relation between NDBI and NDVI index

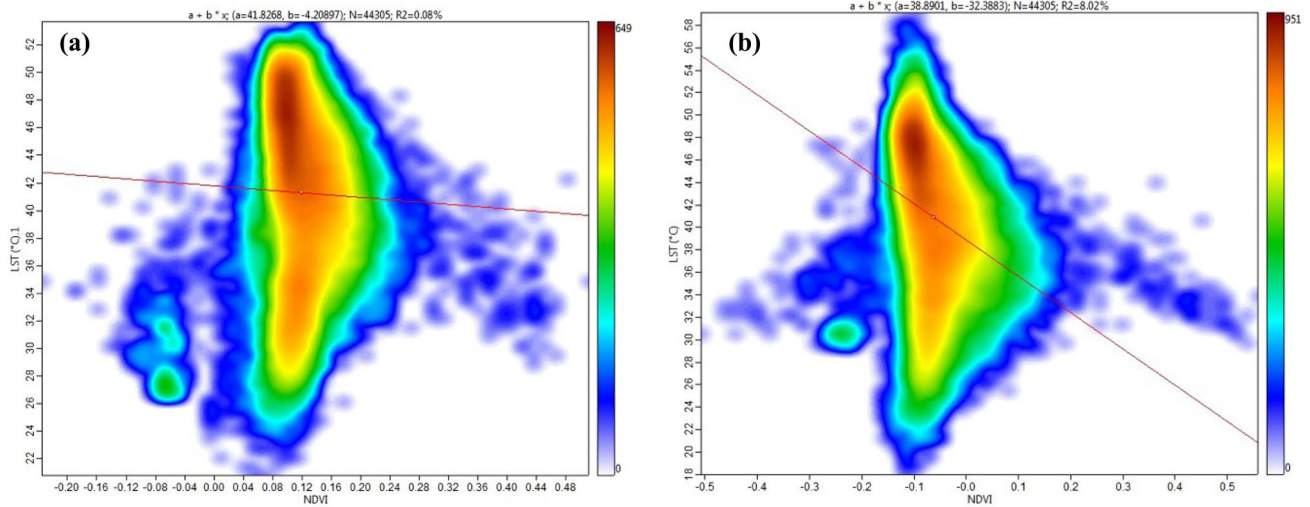
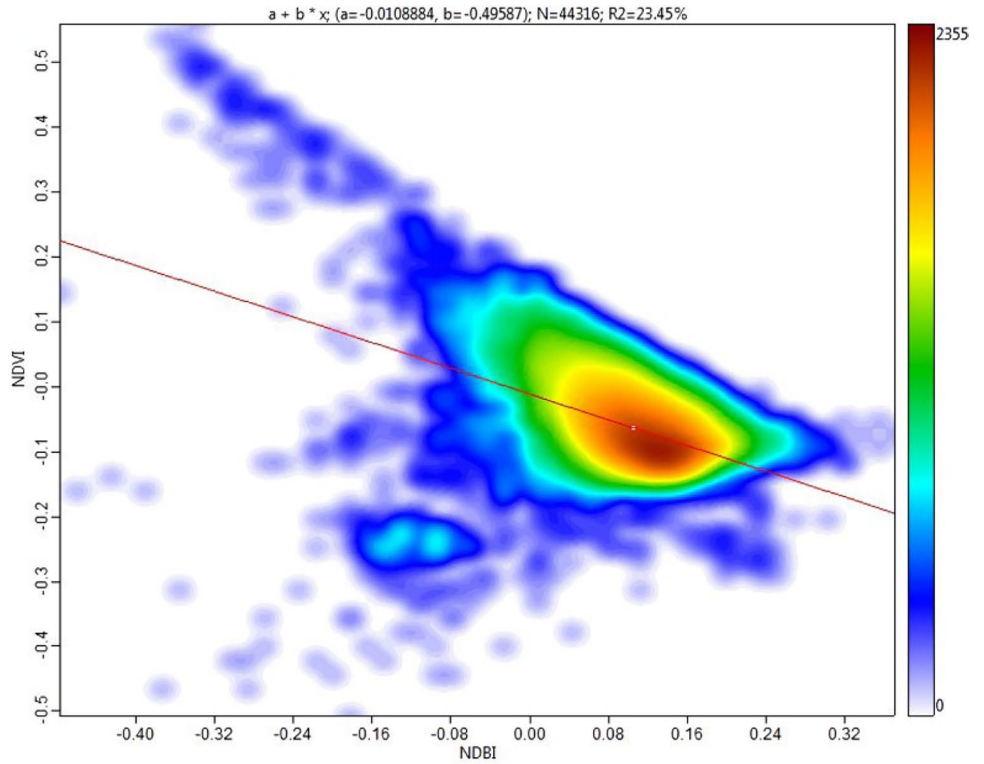


Fig. 12 Relation between LST and NDVI indices in 2001 (a) and 2021 (b)

Table 8 Correlation matrix between LST and other spatial indices for the year 2001

	LST	NDVI	NDWI	NDBI
LST	1	-0.455	0.289	0.322
NDVI	-0.455	1	-0.735	-0.474
NDWI	0.289	-0.735	1	0.482
NDBI	0.322	-0.474	0.482	1

A noteworthy relationship emerges between NDBI and NDWI. While NDBI negatively impacts NDWI, suggesting a decline in water storage with increasing urban areas, the relationship shifts to a positive correlation as water areas expand, and dams are constructed (Fig. 14).

Additionally, NDBI significantly affects LST. Previous studies have demonstrated a strong linear relationship between LST and NDBI (Sun et al., 2012; Tariq et al., 2022).

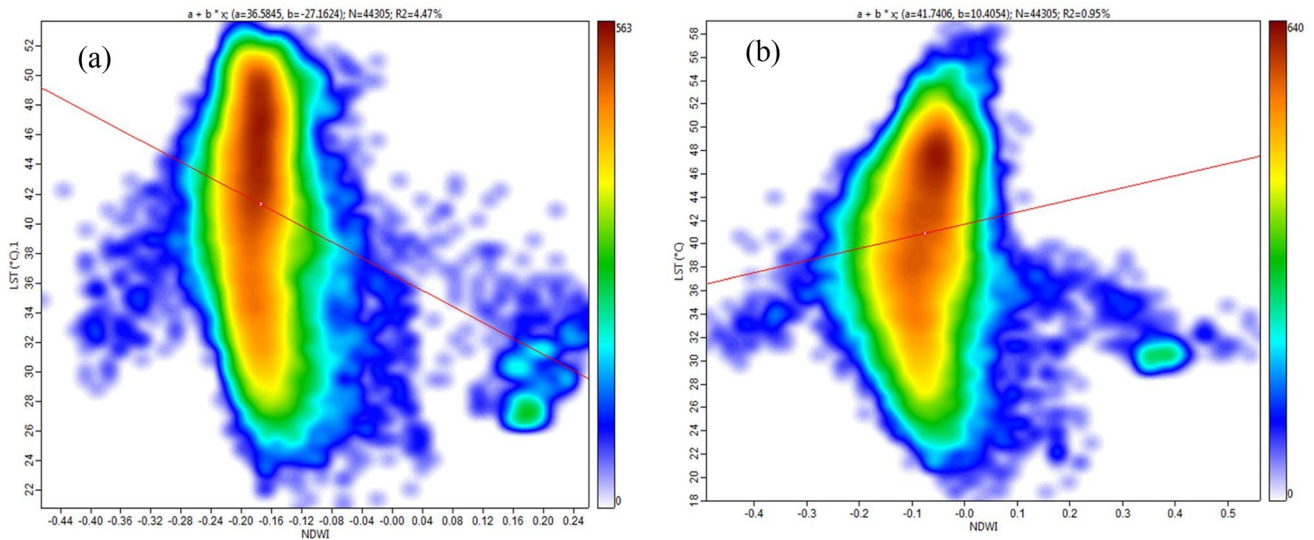


Fig. 13 Relation between LST and NDWI indices in 2001 (a) and 2021 (b)

Fig. 14 Relation between NDWI and NDBI index

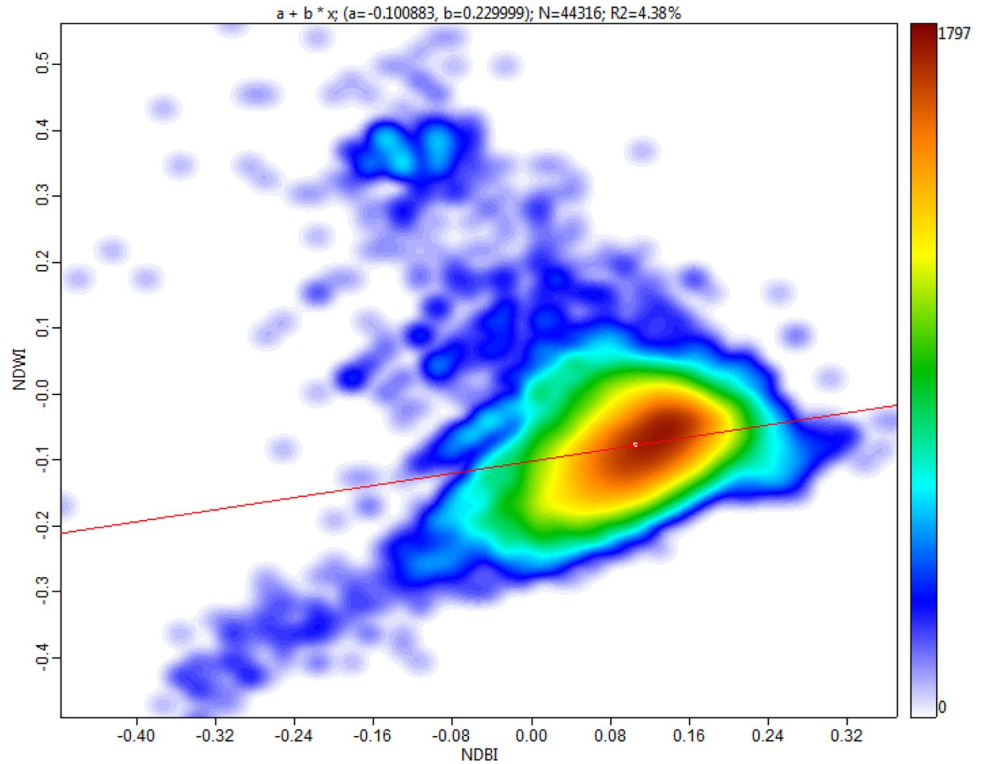


Table 9 Correlation matrix between LST and other spatial indices for the year 2021

	LST	NDVI	NDWI	NDBI
LST	1	-0.209	-0.037	0.208
NDVI	-0.209	1	-0.721	-0.328
NDWI	-0.037	-0.721	1	0.171
NDBI	0.208	-0.328	0.171	1

The correlation value between them is 0.322 for 2001 and 0.208 for 2021 (Tables 8 and 9), indicating a positive association between LST and NDBI (Fig. 15a and b). Given the urban development experienced by Izeh city over; the past two decades, an increase in LST with urbanization is anticipated.

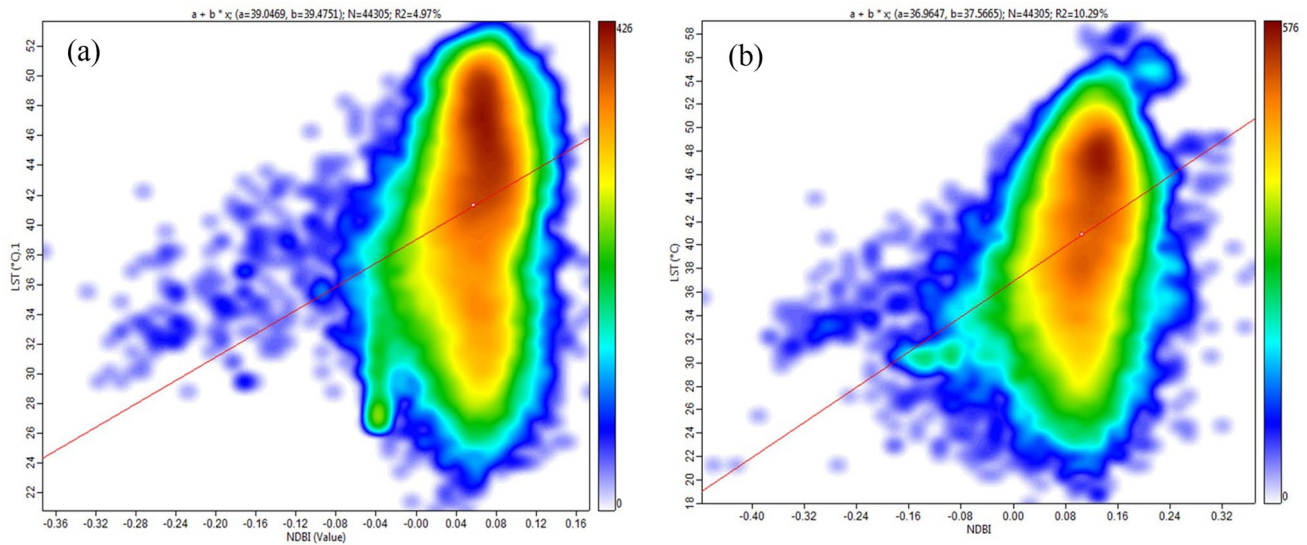


Fig. 15 Relation between LST and NDBI indices in 2001 (a) and 2021 (b)

Conclusion

In this research, an attempt was made to determine the trend of LST changes on LULC in Izeh city. For LULC classification, two pixel-based and object-based methods were used. The ResU-Net model with the FCN approach with Landsat images had higher accuracy compared to the maximum likelihood method despite covering a large area. Comprehensive knowledge and monitoring of land use-land cover, as well as multi-view analysis of the impact of LULC on the thermal environment, help achieve a deeper understanding of the effective mechanisms in increasing the LST in the study area. The trend of LST change in Izeh city shows that the minimum temperature has increased by about 2 °C, while the maximum temperature has decreased by 3 °C per year over 20 years. Spatial and temporal surveys of LST showed hot regions (areas with the highest LST) in the city and wastelands. Therefore, locating these points is essential for studies on sustainable development and environmental monitoring. By comparing the correlation between land use-land cover indices (NDVI, NDWI, and NDBI) and LST under different combinations, it was found that urban areas have a positive and significant correlation with LST. This indicates the effect of urban areas on the increase in LST in Izeh city. Industrial and commercial areas, as well as traffic, significantly influence the degree of human heat emission. Therefore, more trees and parks with thick vegetation should be established in urban areas, and more plants should be planted there.

Gao et al. (2019) utilized the FCN method to classify land cover in mountainous areas, achieving a classification accuracy of 90.6%. In a separate study, Chakhar et al. (2020)

employed various classification algorithms alongside Landsat 8 and Sentinel 2 imagery for crop classification. They experimented with decision trees, diagnostic analysis, support vector machines, nearest neighbors, and group classifiers, yet none of these methods yielded an F1 score exceeding 90%. However, in our current research, the accuracy of classification using the fully convolutional neural network approach and the Res-UNet model surged to 98%.

This research faced limitations as a result of utilizing Landsat 8 images for examining changes detection within the area. Each pixel's spatial resolution was 30 m, indicating the potential benefits of employing imagery featuring a greater spatial resolution, such as Sentinel-2, to enhance the analysis. Furthermore, the temporal resolution could be heightened by incorporating Landsat 9 images.

To enact these measures, meticulous planning is essential for Izeh city to mitigate the escalating temperature. Moreover, the findings of this research will play a pivotal role for urban policymakers and developers in evaluating the extent of land use-land cover alterations in the vicinity, aiming to enhance the future effectiveness and efficiency of the region, and bolster decision-making processes.

Acknowledgements The authors are grateful to the United States Geological Survey (USGS) for providing the Landsat data. Thanks to the reviewers for their comments and suggestions for improving the manuscript.

Author Contribution Razieh Karimian, Kazem Rangzan, Danya Karimi, and Golzar Einali were involved in the overall processing, analysis, and writing. All authors reviewed the manuscript.

Funding No funding was received to assist with the preparation of this manuscript.

Availability of Data and Materials The data and materials that support the findings of this study are available from the corresponding author upon reasonable request.

Declarations

Competing interests The authors declare they have no financial interests.

References

- Adler-Golden, S. M., Acharya, P. K., Berk, A., Matthew, M. W., & Gorodetzky, D. (2005). Remote bathymetry of the littoral zone from AVIRIS, LASH, and QuickBird imagery. *IEEE Transactions on Geoscience and Remote Sensing*, 43(2), 337–347. <https://doi.org/10.1109/tgrs.2004.841246>
- Aguilar-Lome, J., Espinoza-Villar, R., Espinoza, J.-C., Rojas-Acuña, J., Willems, B. L., & Leyva-Molina, W.-M. (2019). Elevation-dependent warming of land surface temperatures in the Andes assessed using MODIS LST time series (2000–2017). *International Journal of Applied Earth Observation and Geoinformation*, 77, 119–128. <https://doi.org/10.1016/j.jag.2018.12.013>
- Al Fugara, A. M., Pradhan, B., & Ahmed Mohamed, T. (2009). Improvement of land-use classification using object oriented and fuzzy logic approach. *Applied Geomatics*. <https://doi.org/10.1007/s12518-009-0011-3>
- Amalisana, B., Rokhmattullah, X., & Hernina, R. (2017). Land cover analysis by using pixel-based and object-based image classification methods in Bogor. *IOP Conf. Series: Earth and Environmental Science*. <https://doi.org/10.1088/1755-1315/98/1/012005>
- Amran, M. A., Samat, N., Hasmadi, I. M., & El-Gamily, H. (2018). Long-term monitoring of the Tigris River water quality parameters using remote sensing techniques. *Journal of Environmental Management*, 206, 907–921. <https://doi.org/10.1016/j.jenvman.2017.11.071>
- Asadi Mehmandosti, E., Adabi, M. H., & Woods, A. D. (2013). Microfacies and geochemistry of the Middle Cretaceous Sarvak Formation in Zagros Basin, Izeh Zone, SW Iran. *Sedimentary Geology*, 293, 9–20. <https://doi.org/10.1016/j.sedgeo.2013.04.005>
- Asgarian, A., Amiri, B., & Sakieh, Y. (2014). Assessing the effect of green cover spatial patterns on urban land surface temperature using landscape metrics approach. *Urban Ecosystem*, 18, 209–222. <https://doi.org/10.1007/s11252-014-0387-7>
- Aslami, F., & Ghorbani, A. (2018). Object-based land-use/land-cover change detection using Landsat imagery: A case study of Ardabil, Namin, and Nir counties in northwest Iran. *Springer International Publishing AG*. <https://doi.org/10.1007/s10661-018-6751-y>
- Ayanlade, A., & Howard, M. T. (2019). Land surface temperature and heat fluxes over three cities in Niger Delta. *Journal of African Earth Sciences*, 151(August 2018), 54–66. <https://doi.org/10.1016/j.jafrearsci.2018.11.027>
- Barnsley, M. J., Møller-Jensen, L., & Barr, S. L. (2001). Inferring urban land use by spatial and structural pattern recognition. *Remote Sensing and Urban Analysis*. <https://doi.org/10.4324/9780203306062>
- Caputo, T., Bellucci Sessa, E., Silvestri, M., Buongiorno, M. F., Musacchio, M., Sansivero, F., & Vilaro, G. (2019). Surface temperature multiscale monitoring by thermal infrared satellite and ground images at Campi Flegrei Volcanic Area (Italy). *Remote Sensing*, 11(9), 1007. <https://doi.org/10.3390/rs11091007>
- Çelik, İ, & Gazioglu, C. (2020). Coastline difference measurement (CDM) method. *International Journal of Environment and Geoinformatics*, 7(1), 1–5. <https://doi.org/10.30897/ijegeo.706792>
- Chakhar, A., Ortega-Terol, D., Hernández-López, D., Ballesteros, R., Ortega, J. F., & Moreno, M. A. (2020). Assessing the accuracy of multiple classification algorithms for crop classification using Landsat-8 and Sentinel-2 data. *Remote Sensing*, 12(11), 1735. <https://doi.org/10.3390/rs12111735>
- Chatterjee, R., & S., Singha, N., Thapaa, Sh., Sharma, D., Kumarb., D. (2017). Retrieval of land surface temperature (LST) from landsat TM6 and TIRS data by single channel radiative transfer algorithm using satellite and ground-based inputs. *International Journal of Applied Earth Observation and Geoinformation*, 58, 264–277. <https://doi.org/10.1016/j.jag.2017.02.017>
- Chen, L., Li, M., Huang, F., & Xu, S. (2013). Relationships of LST to NDBI and NDVI in Wuhan City based on Landsat ETM+ image. *2013 6th International Congress on Image and Signal Processing (CISP)*. <https://doi.org/10.1109/cisp.2013.6745282>
- Choudhury, D., Das, K., & Das, A. (2019). Assessment of land use land cover changes and its impact on variations of land surface temperature in Asansol-Durgapur Development Region, Egypt. *Journal of Remote Sensing and Space Science*, 22, 203–218. <https://doi.org/10.1016/j.ejrs.2018.05.004>
- Coll, C., Galve, J. M., Sanchez, J. M., & Caselles, V. (2010). Validation of landsat-7/ETM+ thermal-band calibration and atmospheric correction with ground-based measurements. *IEEE Transactions on Geoscience and Remote Sensing*, 48(1), 547–555. <https://doi.org/10.1109/tgrs.2009.2024934>
- Cooley, T., Anderson, G. P., Felde, G. W., Hoke, M. L., Ratkowski, A. J., Chetwynd, J. H., Gardner, J. A., Adler-Golden, S. M., Matthew, M. W., Berk, A., Bernstein, L. S., Acharya, P. K., Miller, D., & Lewis, P. (2002). FLAASH, a MODTRAN4-based atmospheric correction algorithm, its application and validation. *IEEE International Geoscience and Remote Sensing Symposium*. <https://doi.org/10.1109/igarss.2002.1026134>
- Dai, J., Li, Y., He, K., & Sun, J. (2016). R-FCN: Object detection via region based fully convolutional networks. In *Proceedings of the Advances in Neural Information Processing Systems, Barcelona, Spain, 5–10*, 379–387.
- Das, N., Mondal, P., Sutradhar, S., & Ghosh, R. (2021). Assessment of variation of land use/land cover and its impact on land surface temperature of Asansol subdivision. *The Egyptian Journal of Remote Sensing and Space Science*, 24(1), 131–149. <https://doi.org/10.1016/j.ejrs.2020.05.001>
- Dhar, R. B., Chakraborty, S., Chattopadhyay, R., & Sikdar, P. K. (2019). Impact of land-use/land-cover change on land surface temperature using satellite data: A Case study of Rajarhat Block, North 24-Parganas District, West Bengal. *Journal of the Indian Society of Remote Sensing*, 47(2), 331–348. <https://doi.org/10.1007/s12524-019-00939-1>
- El-Zeiny, A. M., & Effat, H. A. (2017). Environmental monitoring of spatiotemporal change in land use/land cover and its impact on land surface temperature in El-Fayoum governorate, Egypt. *Remote Sensing Applications: Society and Environment*, 8, 266–277. <https://doi.org/10.1016/j.rsase.2017.10.003>
- Emran, A., Roy, S., Bagmar, M. S. H., & Mitra, C. (2018). Assessing topographic controls on vegetation characteristics in Chittagong Hill Tracts (CHT) from remotely sensed data. *Remote Sensing Applications: Society and Environment*, 11(January), 198–208. <https://doi.org/10.1016/j.rsase.2018.07.005>
- Fikrat, H., Saraskanroud, A., & Alavipanah, K. (2019). Estimation of land surface temperature in Ardabil using Landsat images and evaluation of accuracy and methods of land surface temperature estimation with field data, remote sensing and geographic information system in natural resources, 11th year, 4th issue (pp. 114–136).

- Filgueiras, R., Mantovani, E. C., Dias, S. H. B., Fernandes Filho, E. I., da Cunha, F. F., & Neale, C. M. U. (2019). New approach to determining the surface temperature without thermal band of satellites. *European Journal of Agronomy*, *106*, 12–22. <https://doi.org/10.1016/j.eja.2019.03.001>
- Foody, G. M. (1992). On the compensation for chance agreement in image classification accuracy assessment. *Photogrammetric Engineering & Remote Sensing*, *58*, 1459–1460.
- Gao, L., Luo, J., Xia, L., Wu, T., Sun, Y., & Liu, H. (2019). Topographic constrained land cover classification in mountain areas using fully convolutional network. *International Journal of Remote Sensing*, *40*(18), 7127–7152. <https://doi.org/10.1080/01431161.2019.1601281>
- Ghorbanzadeh, O., Gholamnia, K., & Ghamisi, P. (2022). The application of ResU-net and OBIA for landslide detection from multi-temporal Sentinel-2 images. *Big Earth Data*. <https://doi.org/10.1080/20964471.2022.2031544>
- Gohain, K. J., Mohammad, P., & Goswami, A. (2021). Assessing the impact of land use land cover changes on land surface temperature over Pune city, India. *Quaternary International*, *575*–576, 259–269. <https://doi.org/10.1016/j.quaint.2020.04.052>
- Govind, N., & Ramesh, H. (2019). The impact of spatiotemporal patterns of land use land cover and land surface temperature on an urban cool island: a case study of Bengaluru. *Environmental Monitoring and Assessment*. <https://doi.org/10.1007/s10661-019-7440-1>
- Grimm, N. B., Faeth, S. H., Golubiewski, N. E., Redman, C. L., Wu, J., Bai, X., & Briggs, J. M. (2008). Global change and the ecology of cities. *Science (new York, N.y.)*, *319*(5864), 756–760. <https://doi.org/10.1126/science.1150195>
- Hirasawa, Y., & Urakami, W. (2010). Study on specific heat of water adsorbed in zeolite using DSC. *International Journal of Thermophysics*, *31*, 2004–2009. <https://doi.org/10.1007/s10765-010-0841-6>
- Hu, Y., Zhang, Q., Zhang, Y., & Yan, H. (2018). A deep convolution neural network method for land cover mapping: A case study of Qinhuangdao, China. *Remote Sensing*, *10*(12), 2053. <https://doi.org/10.3390/rs10122053>
- Ibrahim, M., & Abu-Mallouh, H. (2018). Estimate land surface temperature in relation to land use types and geological formations using spectral remote sensing data in Northeast Jordan. *Open Journal of Geology*, *08*(02), 174–185. <https://doi.org/10.4236/ojg.2018.82011>
- Imran, H. M., Hossain, A., Islam, A. K. M. S., Rahman, A., Bhuiyan, M. A. E., Paul, S., & Alam, A. (2021). Impact of Land cover changes on land surface temperature and human thermal comfort in Dhaka City of Bangladesh. *Earth Systems and Environment*, *5*(3), 667–693. <https://doi.org/10.1007/s41748-021-00243-4>
- Jensen, J. R., & Lulla, K. (1987). Introductory digital image processing: A remote sensing perspective. *Geocarto International*, *2*(1), 65–65. <https://doi.org/10.1080/10106048709354084>
- Jimenez-Munoz, J. C., Cristobal, J., Sobrino, J. A., Soria, G., Ninyerola, M., Pons, X., & Pons, X. (2009). Revision of the single-channel algorithm for land surface temperature retrieval from landsat thermal-infrared data. *IEEE Transactions on Geoscience and Remote Sensing*, *47*(1), 339–349. <https://doi.org/10.1109/tgrs.2008.2007125>
- John, J., Bindu, G., Srimuruganandam, B., Wadhwa, A., & Rajan, P. (2020). Land use/land cover and land surface temperature analysis in Wayanad district, India, using satellite imagery. *Annals of GIS*, *26*(4), 343–360. <https://doi.org/10.1080/19475683.2020.1733662>
- Jupp, D. L. B. (1989). The stability of global estimates from confusion matrices. *International Journal of Remote Sensing*, *10*(9), 1563–1569. <https://doi.org/10.1080/01431168908903990>
- Karimi, D., Akbarizadeh, G., Rangzan, K., & Kabolizadeh, M. (2017a). Effective supervised multiple-feature learning for fused radar and optical data classification. *IET Radar, Sonar & Navigation*, *11*(5), 768–777. <https://doi.org/10.1049/iet-rsn.2016.0346>
- Karimi, D., Rangzan, K., Akbarizadeh, G., & Kabolizadeh, M. (2017b). Combined algorithm for improvement of fused radar and optical data classification accuracy. *Journal of Electronic Imaging*, *26*(1), 013017. <https://doi.org/10.1117/1.jei.26.1.013017>
- Kayet, N., Pathak, K., Chakrabarty, A., & Sahoo, S. (2016). Spatial impact of land use/land cover change on surface temperature distribution in Saranda Forest, Jharkhand. *Modeling Earth Systems and Environment*. <https://doi.org/10.1007/s40808-016-0159-x>
- Kruse, F. A. (2004). "Comparison of ATREM , ACO RN, and FL AASH Atmospheric Corrections using Low-Altitude AV IRIS Data of Boulder, Colorado. In *Proceedings 13th JPL Airborne Geoscience Workshop*, Jet Propulsion Laboratory, 31 March ± 2 April 2004, Pasadena, CA, JPL Publication 05-3. <https://popo.jpl.nasa.gov/pub/docs/work>.
- Lakra, K., & Sharma, D. (2019). Geospatial assessment of urban growth dynamics and land surface temperature in Ajmer Region, India. *Journal of the Indian Society of Remote Sensing*, *47*(6), 1073–1089. <https://doi.org/10.1007/s12524-019-00968-w>
- Lambin, E. F., & Ehrlich, D. (1997). Land-cover changes in sub-saharan Africa (1982–1991): Application of a change index based on remotely sensed surface temperature and vegetation indices at a continental scale. *Remote Sensing of Environment*, *61*(2), 181–200. [https://doi.org/10.1016/s0034-4257\(97\)00001-1](https://doi.org/10.1016/s0034-4257(97)00001-1)
- Landis, J. R., & Koch, G. G. (1977). The Measurement of Observer Agreement for Categorical Data. *Biometrics*, *33*(1), 159. <https://doi.org/10.2307/2529310>
- Lewinski, S. (2006). Object-oriented classification of Landsat ETM+ satellite image. *Journal of Water and Land Development*. <https://doi.org/10.2478/v10025-007-0008-4>
- Lillesand, T., Kiefer, R., & Chipman, J. (2003). *Remote sensing and image interpretation* (5th ed., p. 70). Wiley.
- Liu, B., Zhao, X., Fu, X., Yuan, B., Bai, L., Zhang, Y., & Ostadhasan, M. (2020). Petrophysical characteristics and log identification of lacustrine shale lithofacies: A case study of the first member of Qingshankou Formation in the Songliao Basin, Northeast China. *Interpretation*, *8*(3), SL45–SL57. <https://doi.org/10.1190/int-2019-0254.1>
- McFEETERS, S. K. (1996). The use of the Normalized Difference Water Index (NDWI) in the delineation of open water features. *International Journal of Remote Sensing*, *17*(7), 1425–1432. <https://doi.org/10.1080/01431169608948714>
- Mesev, V. (1997). Remote sensing of urban systems: Hierarchical integration with GIS. *Computers, Environment and Urban Systems*, *21*(3–4), 175–187. [https://doi.org/10.1016/s0198-9715\(97\)10003-5](https://doi.org/10.1016/s0198-9715(97)10003-5)
- Moldoveanu, G., & Minea, A. (2019). Specific heat experimental tests of simple and hybrid oxide-water nanofluids: Proposing new correlation. *Journal of Molecular Liquids*, *279*, 299–305. <https://doi.org/10.1016/j.molliq.2019.01.137>
- Moradi, F., Kaboli, H. S., & Lashkarara, B. (2020). Projection of future land use/cover change in the Izeh-Pyon Plain of Iran using CA-Markov model. *Arabian Journal of Geosciences*. <https://doi.org/10.1007/s12517-020-05984-6>
- Nasseri, N. (2019). *Estimating the surface temperature of the earth using single channel algorithm and investigating the effect of land use on temperature changes (case study: Malayer city)*. Environmental Science Studies, 5th period, 2nd issue, summer season (pp. 2477–2482).
- Nguemhe Fils, S. C., Mimba, M. E., Dzana, J. G., Etouna, J., Mounoumeck, P. V., & Hakdaoui, M. (2017). TM/ETM+/LDCM images for studying land surface temperature (LST) interplay with impervious surfaces changes over time within the

- Douala Metropolis, Cameroon. *Journal of the Indian Society of Remote Sensing*, 46(1), 131–143. <https://doi.org/10.1007/s12524-017-0677-7>
- Ozturk, O., Saritürk, B., & Seker, D. Z. (2020). Comparison of fully convolutional networks (FCN) and U-net for road segmentation from high resolution imageries. *International Journal of Environment and Geoinformatics*, 7(3), 272–279. <https://doi.org/10.30897/ijegeo.737993>
- Pal, S., & Ziaul, Sk. (2017). Detection of land use and land cover change and land surface temperature in English Bazar urban centre. *The Egyptian Journal of Remote Sensing and Space Science*, 20(1), 125–145. <https://doi.org/10.1016/j.ejrs.2016.11.003>
- Pordel, F., Ebrahimi, A., & Azizi, Z. (2019). The effect of atmospheric correction methods on the relationship between vegetation indices and canopy cover (Case study: Marjan rangelands of Borujen). *Journal of Geospatial Information Technology*, 7(2), 133–153. <https://doi.org/10.29252/jgit.7.2.133>
- Rangzan, K., Kabolizadeh, M., Zareie, S., Saki, A., & Karimi, D. (2022). The capability of Sentinel-2 image and FieldSpec3 for detecting lithium-containing minerals in central Iran. *Frontiers of Earth Science*. <https://doi.org/10.1007/s11707-021-0941-6>
- Roostaie, S., Alavi, S. A., Nikjoo, M. R., & Valizade Kamran, K. (2012). Evaluation of object-oriented and pixel-based classification methods for extracting changes in an urban area. *International Journal of Geomatics and Geosciences*, 2(3), 738–749.
- Sabins, F. (1997). *Remote Sensing: Principles and Interpretation* (3rd ed., p. 494). Freeman, New York.
- Sherafati, S., Saradjian, M. R., & Rabbani, A. (2018). Assessment of surface urban heat island in three cities surrounded by different types of land-cover using satellite images. *Journal of the Indian Society of Remote Sensing*, 46(7), 1013–1022. <https://doi.org/10.1007/s12524-017-0725-3>
- Soleimani, K., Darvishi, Sh., & Shabani, M. (2018). Investigating the effects of land use changes on temporal and spatial patterns of land surface temperature and thermal islands with a case study of Saqez city. *Geography and Urban Planning*, 30, 37–54.
- Soltani, Z., & Halibian, A. (2019). Analyzing the temporal-spatial changes of urban heat islands and land use with an environmental approach in Shiraz, studies of urban structure and function, 7th year, number 24 (pp. 73–97).
- Sun, Q., Wu, Z., & Tan, J. (2011). The relationship between land surface temperature and land use/land cover in Guangzhou, China. *Environmental Earth Sciences*, 65(6), 1687–1694. <https://doi.org/10.1007/s12665-011-1145-2>
- Tariq, A., Siddiqui, S., Sharifi, A., & Shah, S. H. I. A. (2022). Impact of spatio-temporal land surface temperature on cropping pattern and land use and land cover changes using satellite imagery, Hafizabad District, Punjab Province of Pakistan. *Arabian Journal of Geosciences*. <https://doi.org/10.1007/s12517-022-10238-8>.
- Theres, B. L., & Selvakumar, R. (2022). Comparison of landuse/land-cover classifier for monitoring urban dynamics using spatially enhanced landsat dataset. *Environmental Earth Sciences*. <https://doi.org/10.1007/s12665-022-10242-x>
- Torres, D. L., Turnes, J. N., Soto Vega, P. J., Feitosa, R. Q., Silva, D. E., Marcato Junior, J., & Almeida, C. (2021). Deforestation detection with fully convolutional networks in the Amazon Forest from Landsat-8 and Sentinel-2 images. *Remote Sensing*, 13(24), 5084. <https://doi.org/10.3390/rs13245084>
- Useya, J., & Chen, S. (2018). Comparative performance evaluation of pixel-level and decision-level data fusion of Landsat 8 OLI, Landsat 7 ETM+ and Sentinel-2 MSI for crop ensemble classification. *IEEE Journal of Selected Topics in Applied Earth Observations and Remote Sensing*, 11(11), 4441–4451. <https://doi.org/10.1109/jstars.2018.2870650>
- Weng, Q., Lu, D., & Schubring, J. (2004). Estimation of land surface temperature–vegetation abundance relationship for urban heat island studies. *Remote Sensing of Environment*, 89, 467–483. <https://doi.org/10.1016/j.rse.2003.11.005>
- Williams, D. L., Goward, S., & Arvidson, T. (2006). Landsat. *Photogrammetric Engineering & Remote Sensing*, 72(10), 1171–1178. <https://doi.org/10.14358/pers.72.10.1171>
- Wu, J., Liu, B., Zhang, H., He, S., & Yang, Q. (2021). Fault detection based on fully convolutional networks (FCN). *Journal of Marine Science and Engineering*, 9(3), 259. <https://doi.org/10.3390/jmse9030259>
- Wulder, M. A., White, J. C., & Coops, N. C. (2006). *Identifying and describing forest disturbance and spatial pattern: data selection issues and methodological implications*. Understanding Forest Disturbance and Spatial Pattern (pp. 45–76). <https://doi.org/10.1201/9781420005189-6>
- Xie, S., & Tu, Z. (2015). Holistically-nested edge detection. In: *2015 IEEE international conference on computer vision (ICCV)*. <https://doi.org/10.1109/iccv.2015.164>
- Yoo, C., Han, D., Im, J., & Bechtel, B. (2019). Comparison between convolutional neural networks and random forest for local climate zone classification in mega urban areas using Landsat images. *ISPRS Journal of Photogrammetry and Remote Sensing*, 157, 155–170. <https://doi.org/10.1016/j.isprsjprs.2019.09.009>
- Zha, Y., Gao, J., & Ni, S. (2003). Use of normalized difference built-up index in automatically mapping urban areas from TM imagery. *International Journal of Remote Sensing*, 24(3), 583–594. <https://doi.org/10.1080/01431160304987>

Publisher's Note Springer Nature remains neutral with regard to jurisdictional claims in published maps and institutional affiliations.

Springer Nature or its licensor (e.g. a society or other partner) holds exclusive rights to this article under a publishing agreement with the author(s) or other rightsholder(s); author self-archiving of the accepted manuscript version of this article is solely governed by the terms of such publishing agreement and applicable law.